Ref. Ares(2024)761575 - 01/02/2024

Project number: 101083899

Project Acronym: SHARP-sCO_2

D5.1 Advanced layouts of the SHARP-sCO2 solution

Review version of D5.1 Preliminary layouts and system integration and boundary definitions presented at M6.

Date: 25-01-2024

Author: KTH

This project has received funding from the European Union's Horizon Europe research and innovation programme under grant agreement No 101083899. The content of publication is the sole responsibility of the author(s). The European Commission or its services cannot be held responsible for any use that may be made of the information it contains.

This project has received funding from the European Union's Horizon Europe research and innovation programme under grant agreement No 101083899.

Project contractual details

Project title	Solar Hybrid Air-sCO2 Power Plants
Project Acronym	SHARP-sCO2
Grant Agreement No.	101083899
Project start date	1-11-2022
Project end date	31-10-2025
Duration	36 months
Website	https://www.sharpsco2.eu/

Deliverable details

Number	5.1
Title	Advanced layouts of the SHARP-sCO2 solution– T5.1
Work Package	WP5
Dissemination level	PU
Due date (M)	15
Submission date (M)	15
Deliverable responsible	KTH
Contributing author(s)	S. Guccione, K. A. Kalkavouras
Reviewer(s)	S. Trevisan
Final review and quality approval	25/01/2024

DOCUMENT HISTORY

DATE	VERSION	NAME	CHANGES
11-04-2023	1.0	M. Romero- IME	Initial draft circulated for internal revision
14-04-2023	1.1	J. González-Aguilar-IME	Draft circulated to partners for review
28-04-2023	2.0	M. Romero - IME	Updated version including comments from the consortium – to be submitted
15-01-2024	3.0	S. Guccione, K. A. Kalkavouras - KTH	Draft including techno-economic modelling methodology, system layouts including hybridization with PV and Cogeneration.
25-01-2024	3.1	S. Guccione, S. Trevisan - KTH	Final reviewed version including techno-economic modelling methodology, system layouts including hybridization with PV and Cogeneration.

EXECUTIVE SUMMARY

This report includes functional diagrams describing how to integrate the SHARP-sCO2 components in the new hybrid advanced CSP plants at different scales and including hybridization with PV and heat production via cogeneration. Guidelines for integration both at thermodynamic and operational level (how/where) are presented, alongside with expected operational modes and transients, KPIs are also included and defined to evaluate the system and main components performance.

Specifically, for the virtual lab the following outcomes are presented,

- define the overall boundary conditions and the necessary specifications for the interfaces between the key components, for the overall SHARP-sCO2 cycle "cyber-physical" validation campaign
- evaluate solutions for the integration of disparate components into a whole technical system

In section 2, the Deliverable compiles the preliminary layouts of the integrated system and the identification of the key interfacing points between subsystems. This is an extremely important information because of the cascade effect from upstream to downstream connection in series of the different components. The basic scheme of the "cyber-physical" system is provided and also the upscaled solutions when integrated with the concentrating solar thermal system and the power block. Herewith the importance of some optical parameters and some cycle operation conditions are retained. Considering the impact of off-design typical meteo conditions in sunny areas, it is suggested to use simple regeneration cycle and recompression cycle as the reference sCO_2 ones. Regarding optical interfacing, it is an important issue for the trade-off between solar receiver working temperature and total efficiency of the integrated system. It is observed that an optimum irradiance on aperture value should be between 1,200-1,500 kW/m^2. This value could be incremented to 1,800 kW/m^2 if a high-quality heliostat is used.

In section 3, the list of boundary conditions for virtual lab and upscaled systems is provided together with the identification of tentative preliminary values of key parameters for the main components. Boundary conditions and interfacing operational parameters are agreed for the 50 kWth lab prototype (cyber-physical integration) and two upscaled scenarios for a 10 MWe and a 50 MWe power cycle, assuming the meteo conditions of location of Ouarzazate in Morocco and a solar multiple (SM) of 2.

In Section 4, the main advanced SHARP-sCO2 layouts including PV hybridization and cogeneration are introduced and described. The impact of such additional components over the primary base layout is also discussed. The main operational modes and transitions are described by highlighting their likelihood as well as their impact.

In Section 5, the report introduces the techno-economic and dynamic methodological approach proposed to implement a flowsheeting model and the proposal of initial reference thermodynamic models for the solar field, solar receiver, main heat exchanger, thermal energy storage, electrical heater and power block.

ABBREVIATIONS

BQ: Beam quality of heliostats

CIT: Compressor Inlet Temperature

CSP: Concentrating Solar Power

CST: Concentrating Solar Thermal

DPS: Dense Particle Suspension

EH: Electrical Heater

H&M: Heat and Mass

HEx: Main heat exchanger from hot air to sCO_2 fluid

IR: Irradiance onto Receiver aperture

KPI: Key performance indicator

LCOE: Levelized Cost of Electricity

MCIT: Main Compressor Inlet Temperature

PB: Power Block

PV: Photovoltaic

PCHE: Printed Circuit Heat Exchanger

TES: Thermal Energy Storage

TIT: Turbine Inlet Temperature

Table of contents

1 INTRODUCTION

SHARP-sCO2 aims at developing an integrated system involving core components operating in the cascade stream of the conversion from solar to electricity, as shown in Figure 1. D5.1 focuses on outlining the integration layout schemes for SHARP-sCO2 system, also including advanced hybridized solutions, target operating and boundary conditions. Such layouts should guide some of the decisions on component design to be adopted in WP2 to WP4 providing some harmonization in the power sizing and specifications of working temperatures, pressures and flowrates. Additionally, the insights on the foreseen major operational modes and key transients provides clear indications of the main aspects that should be investigated during the testing and validation campaign of the main components in WPs 2-3-4. Similarly, this also provides indications on the main dynamics to be modelled and investigated during the next actions in WP5.

The analysis is conducted at two levels, the so-called "cyber-physical" system and the up-scaled fully integrated system. The first case relates to a virtual lab to perform a "Cyber-physical emulation" at TRL5 of the different components operating as connected. The second case includes the upscaled flowsheet interfacing with the upstream supply of the concentrated solar thermal power and the downstream integration with the sCO_2 thermodynamic cycle.

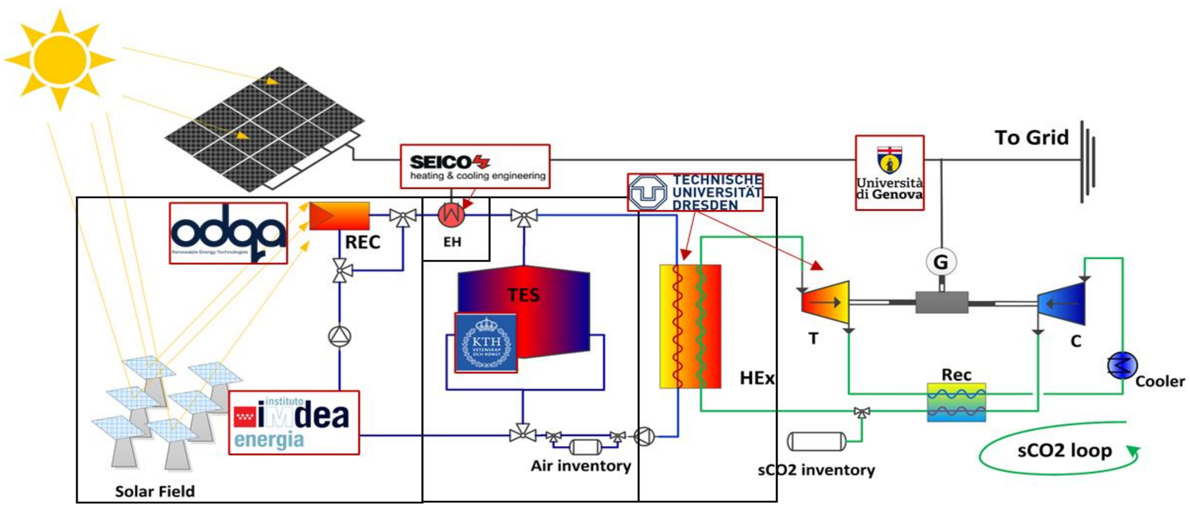

FIGURE 1. BASIC INTEGRATED SCHEME OF THE SHARP-SCO2 HYBRID CONCEPT

2 PRELIMINARY LAYOUTS OF INTEGRATED SYSTEM AND INTERFACING POINTS

2.1 SHARP-sCO2 "cyber-physical" BASIC SCHEME, INTERFACING POINTS AND OPERATION MODES

One of the main objectives of the project is to develop and validate (via a cyber-physical cycle approach) at TRL 5 an innovative air-driven CSP cycle to be hybridized with PV towards LCOE minimisation in WP5. The virtual laboratory is formed by hardware physically located and tested in three different labs. The solar receiver will be tested at the solar field of partner IME in Spain; the EH+TES will be integrated and tested in the lab of KTH in Sweden and finally the HEx will be tested at the sCO2 loop of partner TUD in Germany. Given the distributed configuration of the system, the integration cannot be fully optimized because of constraints imposed by the different test benches. Since an integrated test is also not possible, the validation should be implemented by a harmonized interfacing of inputs and outputs of the different components. Figure 2 represents the flow diagram of the virtual lab with the interfacing point between main components and the operation modes.

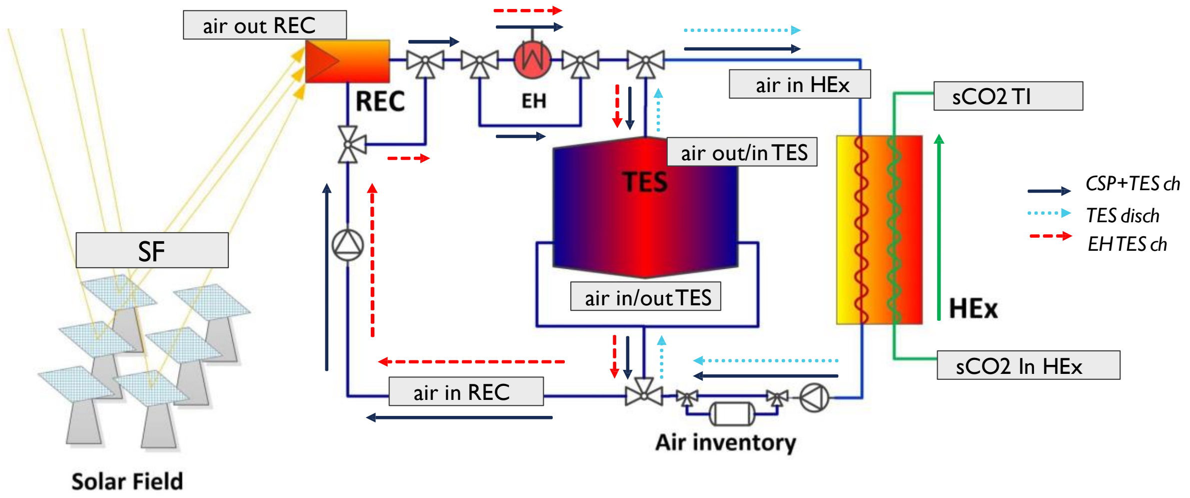

FIGURE 2. BASIC SCHEME OF CYBER-PHYSICAL LAB LAYOUT

The cascade of temperatures between solar receiver/EH and heat exchanger should guarantee a sufficient temperature level at Sco2 TI (temperature input to the thermodynamic cycle) of 650-700 °C by providing temperatures of 800-850 °C upstream of the air loop.

Key interfacing heat and mass (H&M) balance points, including thermal power, flowrate, temperature and pressure (additionally the heat capacity for the TES), are as follows:

- Solar receiver:
  - Air at receiver inlet (Resulting from mixing TES air out+HEx air out)
  - Air at receiver outlet (Inlet to EH)

- Heat exchanger:
    - Air inlet HEx (Resulting from mixing air from EH and/or TES
    - sCO2 TI (Equivalent to Turbine Inlet Temperature+ approx. 20ºC)
    - sCO2 inlet Hex (Resulting from heat recuperation in cycle)
- TES+EH:
    - Air inlet or outlet (depending on charge/discharge cycle)
    - Air outlet or inlet (depending on discharge/charge cycle)

The following operation modes are foreseen in integrated emulation testing:

- Solar receiver+TES charge (black arrow in diagram with bypass of EH), taking place when solar receiver thermal power outlet > PB thermal power inlet and there is an excess of solar thermal power motivated by high DNI and solar multiple assumed for design point. This mode might be also used in PB standby or in the period immediately after sunrise and prior to the start of the PB if TES requires some additional charge by technical reasons.
- Solar receiver+EH+TES charge (black arrow in diagram without bypass of EH). This operation mode is mostly conceived to support solar receiver for charge of TES during the day in periods where DNI is not sufficient, facilitating technical stability of the thermal cycles in the TES.
- EH+TES charge (red arrow in diagram), required to prepare TES for the next operation mode, start-up or transients, in the event that solar receiver is not active
- TES discharge (light blue arrow in diagram), required for cold start-ups or daily startup ramps of PB and for periods requiring extended operation of PB after sunset or during transients when solar field is not active.

2.2 SHARP-sCO2 upscaled system: interfacing with solar field and power block

For upscaled fully integrated systems, the upstream integration takes place at the solar receiver aperture, involving optical and thermal optimization of losses, being air inlet and outlet specifications together with the required receiver thermal efficiency, the key design elements. Regarding downstream integration with the selected sCO_2 power block, the key element of interface is the primary heat exchanger air to sCO_2.

Even though sCO_2 cycle presents a high efficiency potential, up to 50% in some operational conditions, it has been also reported to be very sensitive to TIT (HEx) and CIT (meteo- ambient air T) (Reyes-Belmonte et al., 2016). Despite its simplicity, it is a highly regenerative cycle subject to a variety of solutions of internal heat management involving significant heat exchangers between fluids with dissimilar thermal properties and flowrates. Various configurations of the sCO_2 Brayton cycle have been proposed in the literature implying some modifications in the interfacing of TIT and CIT with sCO_2 In Hex and sCO_2 TI. From previous experience of partner IME (Chen et al., 2021), as many as six different cycle layouts are herewith proposed for the preliminary integrated flowsheets of the upscaled integrated systems (represented in Figures 3 to 8, for simple regeneration, recompression, precompression, intercooling, partial cooling and split expansion) and making use of a dry cooling system.

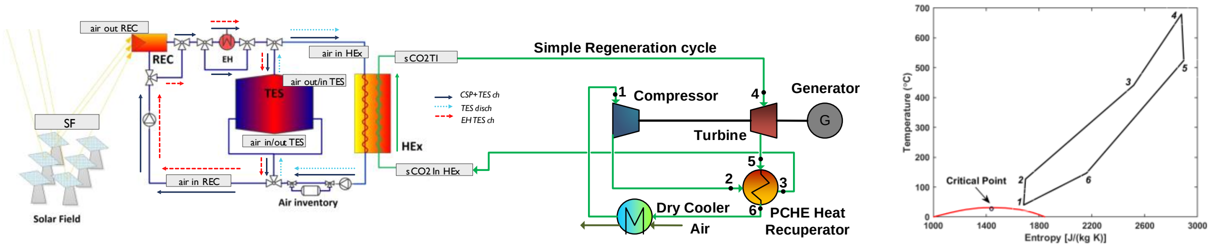

FIGURE 3. INTEGRATION WITH SIMPLE REGENERATION SCO_2 BRAYTON CYCLE AND CORRESPONDING T-S DIAGRAM.

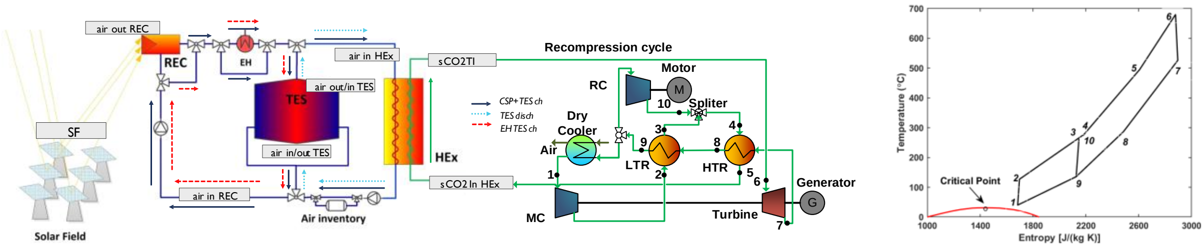

FIGURE 4. INTEGRATION WITH RECOMPRESSION SCO_2 BRAYTON CYCLE AND CORRESPONDING T-S DIAGRAM.

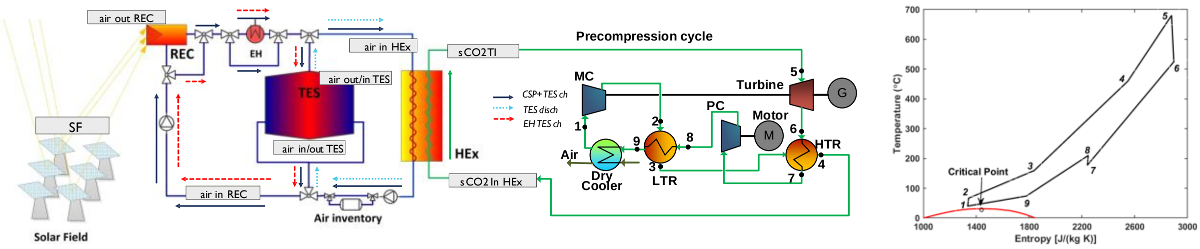

FIGURE 5. INTEGRATION WITH PRECOMPRESSION SCO_2 BRAYTON CYCLE AND CORRESPONDING T-S DIAGRAM.

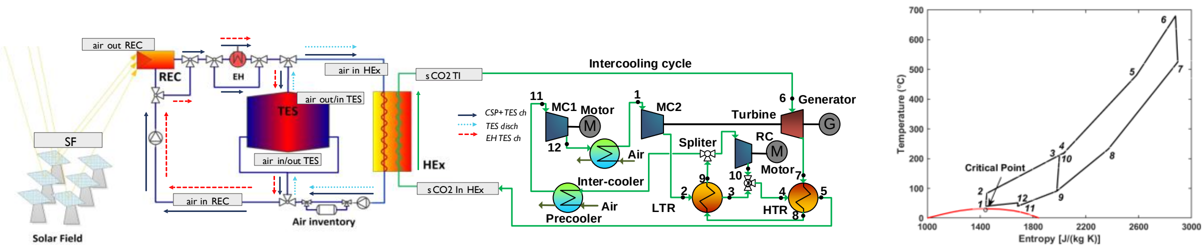

FIGURE 6. INTEGRATION WITH INTERCOOLING SCO_2 BRAYTON CYCLE AND CORRESPONDING T-S DIAGRAM.

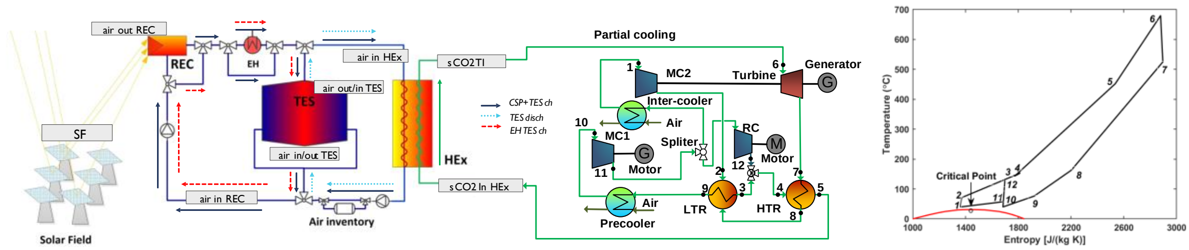

FIGURE 7. INTEGRATION WITH PARTIAL COOLING sCO_2 BRAYTON CYCLE AND CORRESPONDING T-S DIAGRAM.

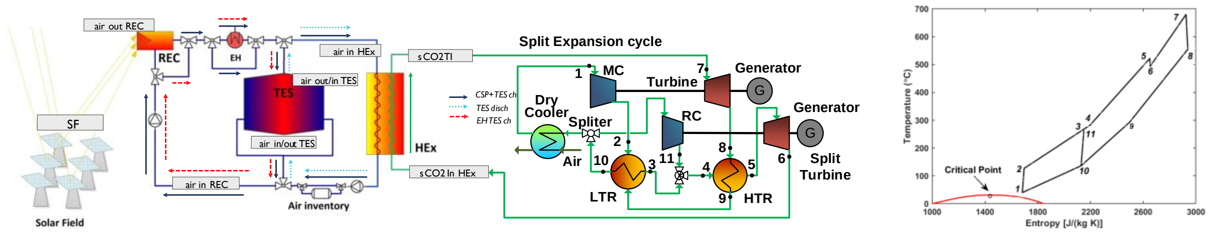

FIGURE 8. INTEGRATION WITH SPLIT EXPANSION sCO_2 BRAYTON CYCLE AND CORRESPONDING T-S DIAGRAM.

Simple regeneration cycle

Figure 3 shows the configuration and corresponding T-s diagram of simple regeneration sCO_2 Brayton cycle, which incorporates a recuperator in the original Brayton cycle to recover the waste heat. Since the heat regeneration is generally required, the simple regeneration, instead of the original cycle, is always considered as the reference layout, and more sophisticated layouts can be derived from it. In this cycle, state 1 corresponds to the compressor inlet, which is near the CO_2 critical point. In the compressor, the sCO_2 is compressed to high pressure (point 1 to 2) and preheated in the printed circuit heat exchanger (PCHE) recuperator to state 3. Then the sCO_2 is heated to the maximum temperature by HEx. From the HEx, the high-temperature and high-pressure sCO_2 (state 4) expand in the turbine to transform the fluid energy into rotational work of shaft which connects the compressor, turbine and generator. The exhaust fluid (state 5) is subsequently cooled down in the recuperator (state 6) and dry air cooler, where the compressor inlet temperature is reached by rejecting energy to the ambient.

Recompression cycle

Though the introduction of recuperator recovers much waste heat, the cycle efficiency is still limited by the pinch-point problem, which means that the temperature difference at some points may be smaller than the minimum temperature difference. This is caused by specific sCO_2 thermo-physical properties. In the low-temperature part of the recuperator, the specific heat in the cold stream is nearly two times greater than that in the hot stream. To solve the pinch-point problem, the recompression cycle is proposed by decreasing the mass flow rate of the high-pressure stream. Compared to the simple regeneration cycle, the recompression cycle adds an additional compressor (recompressor) and splits the low-pressure stream by dividing the regenerator into two parts: the low temperature recuperator (LTR) and the high temperature recuperator (HTR) as shown in Figure 4.

Simple regeneration cycle and recompression cycle are the two options selected as benchmark for the upscaled analysis in the project, though other more complex solutions might be eventually analysed as well, as represented by precompression, intercooling, partial cooling and split expansion in Figures 5 to 8. In the end, the recompression and precompression cycle represent two possible ways to solve the pinch-point problem in the simple regeneration cycle. The intercooling, partial cooling and split expansion cycle are all derived from the recompression cycle, the difference between them being that the intercooling and partial cooling have an additional precompressor and intercooler but in different positions, while the split expansion cycle has an additional split expander.

TABLE 1. COMPARISON OF SIX CYCLE PERFORMANCES UNDER THEIR OPTIMAL DESIGN CONDITIONS.

Configuration	Cycle efficiency (%)	Specific work (kJ/kg)	The temperature difference of hot fluid in HEx (°C), Tout-Tin
Simple regeneration	43.63	131.04	216.62
Recompression	50.00	116.60	158.71
Precompression	48.56	132.91	196.92
Intercooling	52.11	130.67	174.28
Partial Cooling	49.46	141.91	205.26
Split Expansion	49.54	115.26	160.26

From a previous analysis carried out by IME (Chen et al, 2021), using a Dense Particle Suspension (DPS) inlet temperature of 700 °C as the equivalent to sCO_2 TI in our current Hex in SHARP-sCO2 project, see Table 1, it could be realized that the intercooling cycle presents the highest cycle efficiency (52.11%), followed by recompression cycle, split expansion cycle and intercooling cycle. The partial cooling system has the largest specific work (141.91 J/kg) and the split expansion cycle leads to the lowest specific work. In terms of the thermal ability of integration with TES, both the temperature differences of heat transfer fluid in HEx in simple regeneration cycle and partial cooling cycle are larger than 200 °C, while such HEx temperature difference in recompression cycle is only 158.71 °C. The performance of split expansion cycle is similar to the recompression cycle. Compared to recompression cycle, the intercooling cycle contributes to better performance in terms of all these three aspects, while the partial cooling cycle presents less cycle efficiency. It is pointed out that introducing intercooling with multistage main compression is beneficial to increase the specific work and HEx temperature difference, but not always good for the cycle efficiency.

However, an important additional result is that all cycles are equally negatively impacted when working at off-design conditions below 700 °C as shown in Figure 9.

Variations of T_{air} and its key role in the dry cooling system are leading to more significant impacts on cycle performance degradation than the reduction in sCO2 TI. When sCO2 TI is 240 °C less than the design value, most configurations can still provide almost 50% of nominal power with about 30% cycle efficiency. However, for the complex systems presenting higher design-point cycle efficiency and specific work, such as intercooling and partial cooling cycles, their off-design performance exhibits a larger deterioration with increasing Tair. The closer the design-point fluid state at the inlet of the main compressor is to the critical point of CO_2, the better the cycle design performance, but the more sensitive the cycle off-design performance is to the increase in Tair. As presented in Figure 10, for sunbelt regions where ambient air temperatures easily surpass 35 °C, the selection of simple regeneration and recompression cycles are providing a more stable performance. Because of that, it is recommended to select those two cycles as the reference for the upscaled integrated analysis in SHARP-sCO2 project.

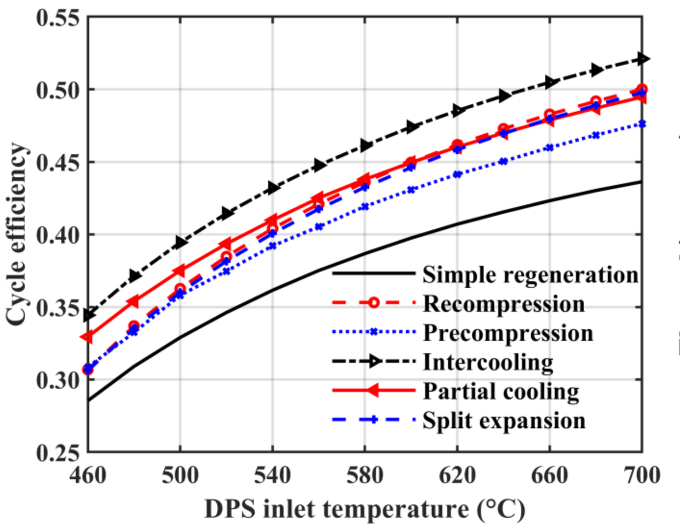

FIGURE 9. VARIATION OF CYCLE EFFICIENCY VERSUS SCO2 TI AT THE EXIT OF HEX (EQUIVALENT TO DPS INLET TEMPERATURE IN CHEN ET AL., 2021) AT DESIGN POINT OF TIT 680 °C AND OFF-DESIGN

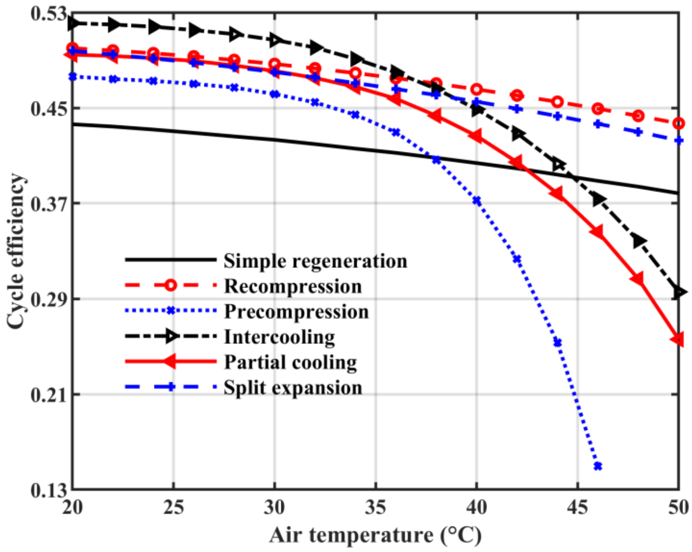

FIGURE 10. VARIATION OF CYCLE EFFICIENCY WITH AMBIENT AIR TEMPERATURE FOR A SYSTEMS WITH DRY COOLING (TIT: 680 °C; CIT: 20 °C)

2.3 IMPORTANCE OF UPSTREAM (OPTICAL) AND DOWNSTREAM (THERMODYNAMIC CYCLE OPERATION CONDITIONS)

The integration of the CST system and the power block, introduce two contradictory interests in terms of optimization of the operational conditions. The increment of TIT in the power block directly increases the cycle efficiency, being necessary to go up, close to 700 °C, to make the most of the Sco2 benefits. However, the increment of temperature in the thermodynamic cycle provokes a cascade of effects, positive and negative, in the rest of components of the CST plant, like the solar receiver or the heliostat field. Therefore, an integral system-level analysis and optimization is essential to improve the solar-to-electricity conversion efficiency of CSP. The incident irradiance on the receiver aperture (IR) and temperature of the air at the receiver outlet or inlet to the HEx (Tair in HEx), both at the nominal conditions, are key parameters that determine the optical and thermodynamic integration of main subsystems. These two parameters affect the efficiency of solar field, receiver and power block simultaneously, but with opposite patterns of influence. In particular, determining proper IR and Tair In HEx is important for the CSP system integrated with a solar receiver and sCO_2 Brayton cycle due to their specificities. On one hand, the high Tair In HEx requirement from sCO_2 Brayton cycle forces the solar receiver to operate at high solar concentration, which in turn leads to designs with smaller aperture area for the same power inlet (high IR) and consequently lower thermal losses. On the contrary, this reduction of aperture area can lead to high spillage losses in the heliostat field as the optical interception of the incident rays is constrained. Although the efficiency of solar receiver could reach above 80% in our project, the corresponding low optical efficiency of solar field due to high spillage losses may offset the gains in whole system thermal efficiency.

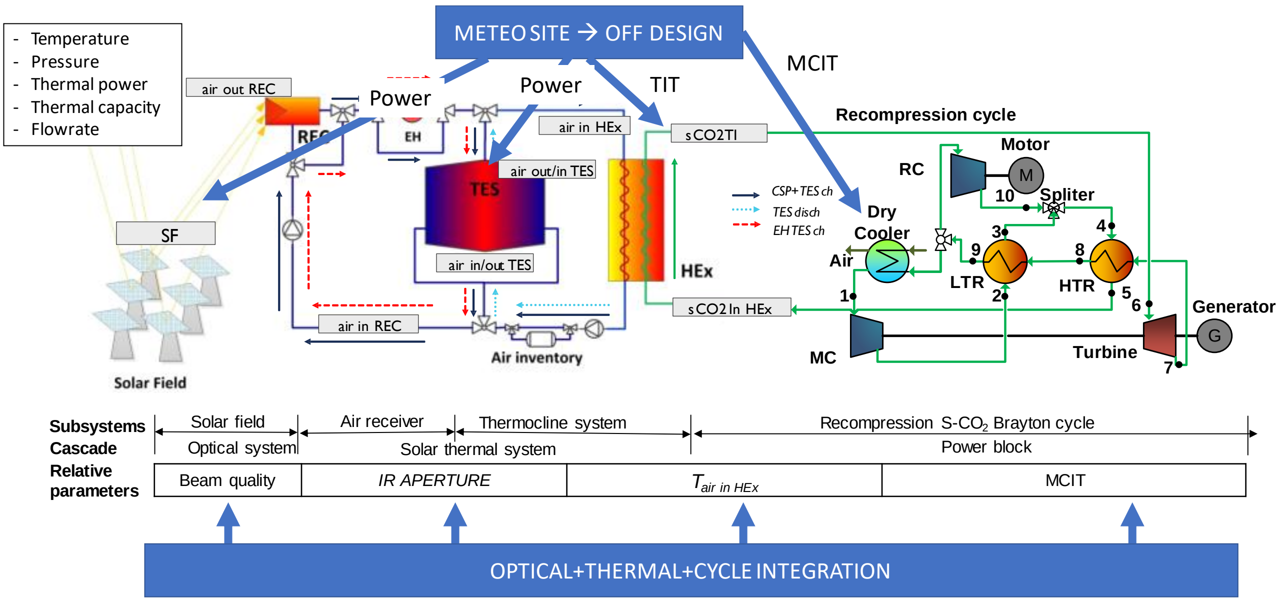

FIGURE 11. SCHEMATIC DIAGRAM OF THE INTEGRATED SYSTEM INCLUDING SOLAR FIELD, RECEIVER, TES+EH AND THE RECOMPRESSION SCO_2 BRAYTON CYCLE. MC AND RC REFER TO MAIN COMPRESSOR AND RECOMPRESSOR RESPECTIVELY; HEX REFERS TO THE PRIMARY HEAT EXCHANGER OF AIR TO SCO_2; HTR AND LTR REFER TO HIGH AND LOW TEMPERATURE RECUPERATOR RESPECTIVELY; IR REPRESENTS THE INCIDENT IRRADIANCE ON THE RECEIVER APERTURE, TAIR MEANS THE AIR TEMPERATURE AT THE RECEIVER OUTLET OR AT HEX INLET AND MCIT REFERS TO THE MAIN COMPRESSOR INLET TEMPERATURE (ADAPTED FROM CHEN ET AL., 2022).

Figure 11 is an adaption from a background analysis carried out by IME (Chen et al., 2022) considering the influence of some parameters with key influence in the subsystems cascade. Apart from the H&M parameters already referred in section 2.1 for the cyber-physical system like temperature, pressure, thermal power, thermal capacity and flowrate in the different streams, other important parameters to be kept in mind for the boundary conditions selection are beam quality of heliostats and IR (optical); IR and Tair in HEx (thermal conversion in solar loop) and Tair In Hex and MCIT (thermodynamic cycle). In addition, the selection of the site and meteo conditions clearly influence solar field power, capacity factor, TIT and MCIT.

Of particular importance for the selection of the boundary conditions of solar receiver in the project is the IR onto receiver aperture.

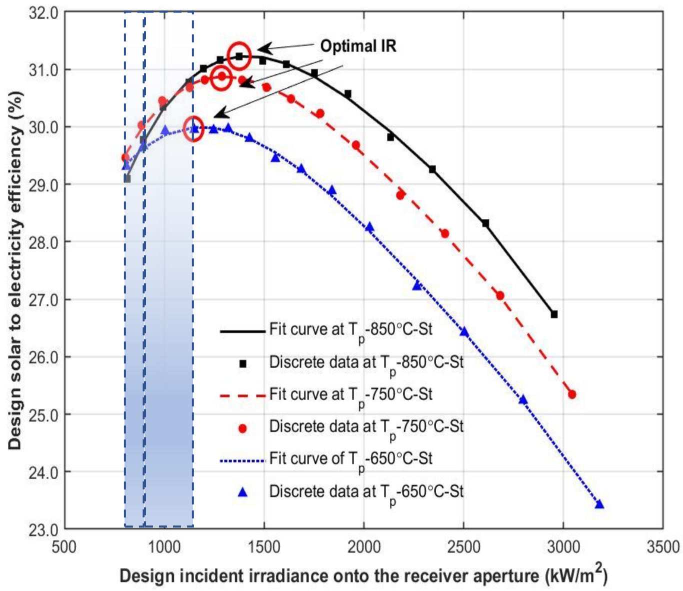

FIGURE 12. TOTAL DESIGN EFFICIENCY VERSUS IR FOR DIFFERENT TP (RECEIVER AIR OUTLET TEMPERATURE IN OUR PROJECT) FOR THE STANDARD CASE (ST, BASE HELIOSTAT STANDARD BEAM QUALITY BQ AND MCIT OF 40 ºC).

Figure 12 shows the convex parabolic variation of η_{total_design} versus *IR* with three *Trec out* conditions (Tp). For each T_p, there is an optimal *IR* that maximizes η_{total_design} due to the trade-off between the advantage of η_{rec_design} and the disadvantage of η_{sf_design} as the *IR* increases. For *IR* between 1,250 and 1,380 kW/m^2, a balance is achieved between the increased optical spillage losses from the solar field and the reduced thermal losses from the solar receiver. Notably, the η_{total_design} ranking among the selected three T_p conditions changes according to the range of *IR*. For *IR* between 800 and 900 kW/m^2, T_p has negligible impact on η_{total_design}; between 900 to 1,200 kW/m^2, there is no obvious difference in η_{total_design} for T_p above 750 ºC. When *IR* is above 1,300 kW/m^2, system operating at T_p of 850 ºC starts to perform with the highest η_{total_design}, followed by the system operating at 750 ºC and then 650 ºC. This variation pattern emphasizes the importance of selecting *IR* properly, allowing to achieve conversion efficiencies well above 30% at design point. The benefits from power block when increasing T_p on η_{total_design} only can be gained with a high *IR* (over 1,000 kW/m^2), which is over the attainable incident flux range of external receivers.

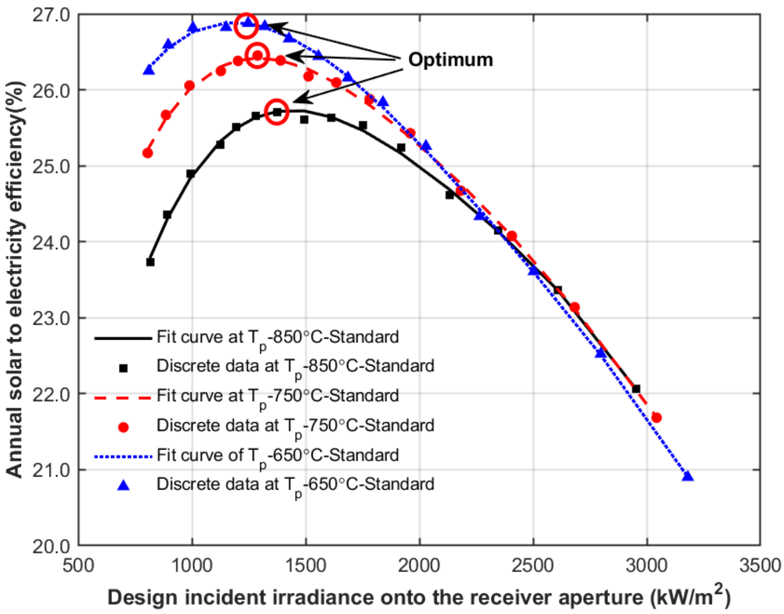

FIGURE 13 VARIATION OF η_{TOTAL_ANNUAL} WITH *IR* IN THREE T_P (RECEIVER AIR OUTLET TEMPERATURE IN OUR PROJECT) FOR THE STANDARD CASE (STANDARD, BASE HELIOSTAT BQ AND MCIT OF 40 ℃). THE ANNUAL EFFICIENCY DOES NOT INCLUDE THE PARASITIC, STORAGE LOSSES AND POWER BLOCK START-UP AND SHUT-DOWN LOSSES.

Annual operation of a fully integrated CSP plant involves frequent periods working at part-load that may imply that the design conditions for optimal annual performance do not necessarily coincide with those for optimal design performance. Fig. 7 displays η_{total_annual} as a function of *IR* at three different T_p. Similar to η_{total_design}, η_{total_annual} also presents a convex parabolic variation versus *IR* at each T_p. The same optimal *IR* maximizes both η_{total_design} and η_{total_annual}. However, the η_{total_annual} ranking is the exact opposite of η_{total_design} ranking for these three T_p conditions. The highest and the lowest η_{total_annual} correspond to 650 ºC and 850 °C, respectively. When *IR* is below 1,000 kW/m^2, a 2.52% reduction in η_{total_annual} is found for T_p at 850 ℃ compared to 650 °C while their η_{total_design} is very similar. However, a converging trend in η_{total_annual} is observed for different T_p when *IR* is over 2,200 kW/m^2. This conflict between the system performance at design point and annual conditions highlights the necessity of off-design and annual simulations to determine the appropriate T_p (in our case receiver outlet air temperature).

In conclusion, after analysing the trade-off between solar receiver working temperature and total efficiency of the integrated system, it is observed that an optimum IR on aperture value should be between 1,200-1,500 kW/m^2. This value could be incremented to 1800 kW/m^2 if a high-quality heliostat is used.

3 CYBER-PHYSICAL DEMO AND UPSCALING BOUNDARY CONDITIONS AT INTERFACING POINTS

From the previous discussions and layouts proposed in section 2, the following boundary conditions and interfacing operational parameters are agreed for the 50 kWth lab prototype (cyber-physical integration) and two upscaled scenarios for a 10 MWe and a 50 MWe power cycle, assuming the meteo conditions of location of Ouarzazate in Morocco and a solar multiple (SM) of 2. As the key components of the Lab prototype are still under conceptual design review, there might be changes and modifications, to be updated in the revision of this deliverable by month 15.

TABLE 2. BASIC SPECIFICATIONS OF THE SITE FOR UPSCALED SYSTEMS

General plant specification	Value
Location	Ouarzazate, Morocco (30.9°N, 6.93°W)
Design point	Spring equinox (21st March) noon
Design DNI (W/m^2)	900
Solar multiple	2
Power block capacity (MW)	10/50

TABLE 3. BOUNDARY CONDITIONS FOR CYBER-PHYSICAL LAB PROTOTYPE AND UPSCALED SYSTEMS

	Lab Prototype	Upscaling 1 – Single tower	Upscaling 2 – Multi tower (tbd)
sCO_2 power cycle	//	10 MW_e	50 MW_e
sCO_2 power cycle efficiency	//	0.35-0.50	0.37-0.50
Air loop maximum temperature	850 °C	850 °C	850 °C
Air loop minimum temperature	400 °C	400 °C	400 °C
Air to sCO_2 HEX th. load	50 kW_t	~30 MW_{th} → x600	~135 MW_{th} → x2700 (x4.5)
Receiver th. Power	50 kW_t	~60 MW_{th} (SM=2) → x1200	~270 MW_{th} (SM=2) → x5400 (x4.5)
TES energy capacity	50 kWh_t	~300 MWh_{th} (10h) → x6000	~1350 MWh_{th} (10h) → x27000 (x4.5)
TES power (ch & disch)	50 kW_t	~30 MW_{th} → x600	~135 MW_{th} → x2700 (x4.5)
EH nominal power	50 kW_e	~30 MW_{th} → x600	~135 MW_{th} → x2700 (x4.5)

#: based on preliminary sizing estimations
#: upscaling ratio vs lab (and upscaling 1 for the case of upscaling 2)

TABLE 4. TARGET RANGE AND LAB LIMITS OF KEY INTERFACING PARAMETERS FOR SOLAR RECEIVER, ELECTRICAL HEATER, THERMAL ENERGY STORAGE AND MAIN HEAT EXCHANGER AIR TO sCO_2.

RECEIVER	Target range	Lab limits
Th. power solar field [kW]	62.5 (min solar flux to aperture)	75
Th. power receiver [kW]	**50**	50
Air temperatures [°C]	400 – **800**	800
Air flow rate [kg/s]	0.166	-
Max air pressure [barg]	<2	2
Solar concentration at aperture [kW/m^2]	1,200-1,500	2,500
EH**	**Target range**	**Lab limits**
Th. Power [kW]	0 – 50	0 – tbd
Air temperatures [°C]	400 – **850**	20 – 850
Air flow rate [kg/s]	0.12	0.1*
Air pressure [bar]	1+	1+
Voltage [V]	**6000**	6000
Other specifications	**3 phase - AC**	-

**EH considered as installed within KTH solar lab

TES	Target range	Lab limits
Th. Power [kW]	0 – 50	-
Th. energy capacity [kWh]	**50**	-
Air temperatures [°C]	400 – **800**	ambient – 750 (valves)/850 (current EH)
Air flow rate charge [kg/s]	0.12	0.1* (*higher for short periods – buffer)
Air flow rate discharge [kg/s]	0.12	0.1*
Air pressure [bar]	1+	1+
HEx	**Target range**	**Lab limits**
Th. Power [kW]	**50**	-
Air temperatures [°C]	400 – **700**	20 - 700
sCO2 temperature [°C]	400 – **650**	Currently max 300
Air flow rate [kg/s]	0.15	tbd
sCO2 flow rate [kg/s]	0.16	0.2-0.5
Air pressure [bar]	1+	1+
sCO2 pressure [bar]	200	200

4 ADVANCED SHARP-sCO2 SYSTEM LAYOUTS

Figure 14 shows the schematic of an air based CSP plant with air packed bed energy storage and sCO2 power cycle. During daytime, the heliostat field concentrates the solar radiation on the air receiver, placed on top of the tower, to convert the power collected by the heliostat field into thermal power with operating temperatures ranging between ~400 and 800 ◦C. The HTF flows then in a packed bed TES to store the thermal power produced. The TES decouples the electricity production from the intermittent solar-based heat production. The thermal-to-electric reconversion is realized by using a sCO2 power block. During nighttime, the TES is discharged, so air flows into the packed bed TES and then transfer the thermal power to the sCO2 through the air-to-sCO2 heat exchanger, targeting a Turbine Inlet Temperature (TIT) of 750 ◦C.

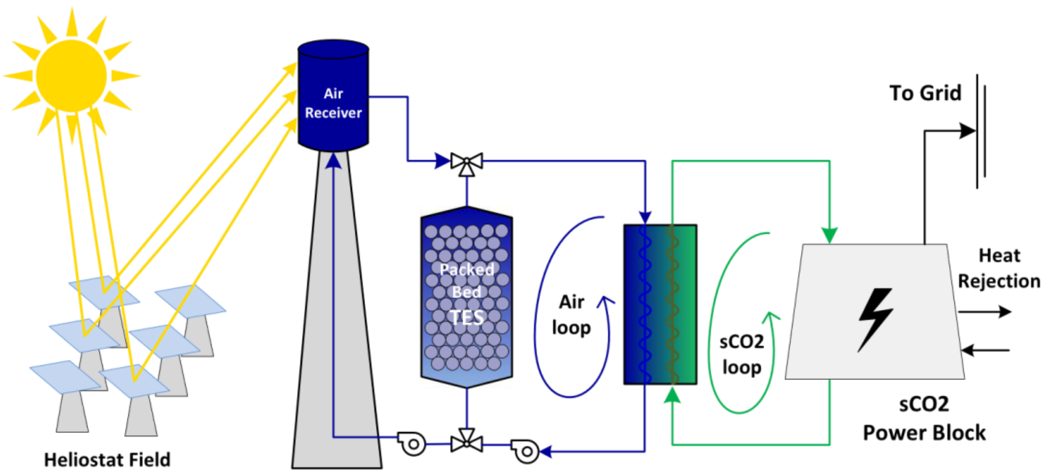

FIGURE 14. LAYOUTS OF AIR-BASED CSP SYSTEM

4.1 HYBRIDIZATION WITH PV

Hybrid systems including connection with solar photovoltaic (PV) have been identified as a viable solution to reduce the cost of electricity of CSP plants while maintaining the flexibility and high-capacity factors granted by the TES unit. The costs of a hybrid CSP-PV facility could be 25% lower than an equivalent-sized CSP-only plant. Figure 15 shows the schematics of the hybridization with PV proposed for air-based CSP plants presented previously in Figure 14. These proposed hybrid plants operate in the following manner: during daylight hours, the PV system generates electricity, which is supplied to the grid until it reaches the grid connection limit. If the PV system generates excess power beyond this limit, the electric heater charges the TES until PV production falls below the limit or electricity is stored in the BESS system. Simultaneously, the CSP plant's solar field operates to produce thermal power, which is stored in the TES. The plant's control logic enables different operating modes based on solar irradiance, TES charge status, BESS charge status and PV electricity production. To bridge the gap between PV production and the grid connection limit, the CSP plant utilizes the stored energy in the TES to generate electricity until either the storage is empty, or the PV production once again reaches the maximum power injectable to the grid. This hybridization between PV and CSP, involving power exchanges through electric heaters, is referred to as "active hybridization", distinguishing it from the practice of "co-locating" PV and CSP plants. In co-location scenarios, PV and CSP plants share the same grid connection point, with a portion of PV production dedicated solely to fulfilling the parasitic consumption needs of the CSP plant. Figure 15a shows a state-of-the-art PV plant hybridized with a central tower CSP plant with an air receiver, an air-driven packed bed TES system, a BESS system and a sCO2 Brayton power block. The hybridization between PV and CSP is realized by employing an electric heater for air that allows storing the electricity produced in excess by the PV field as thermal energy. However, this electric heater is operated in parallel to the CSP system as presented in the current layout. In other upscaling scenarios of hybrid PV-CSP systems, the electric heater could operate also in series with the CSP system for heat upgrading purposes. In the power plant layout shown in Figure 15b, the PV field can inject directly into the grid the electricity produced, or when the production exceeds the maximum injectable power, the excess can be stored as thermal energy through an electric heater and a packed bed TES system. The thermal-to-electric reconversion is realized by using a sCO2 power block. The PV and CSP plants actively hybridized in Figure 15a become two power plants "co-located" if the EH installed capacity is zero.

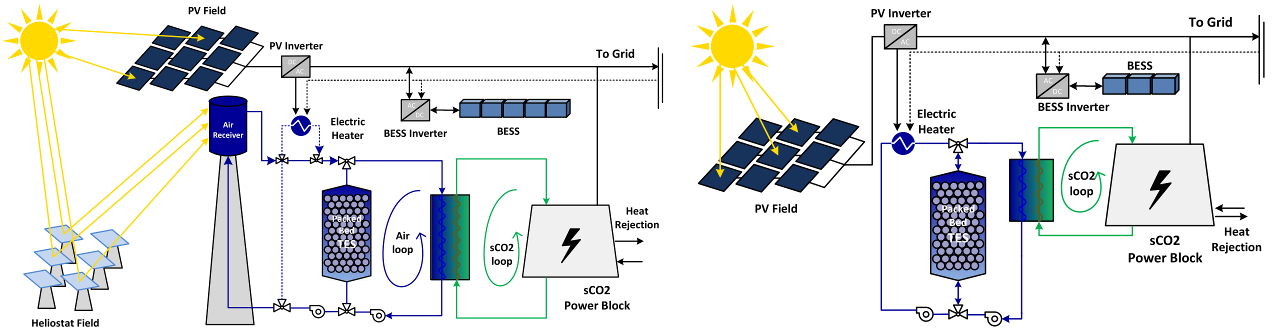

FIGURE 15. LAYOUTS OF HYBRID PV-CSP SYSTEM AND PV-EH-TES SYSTEM

4.2 COGENERATION

Another potential layout of the hybrid PV-CSP power plant previously presented, could include the generation of heat in different temperature levels. Cogeneration could enable a more efficient use of the power plant's output and resources, and be able to meet combined energy demands, while flexibility and dispatchability are also increased. Nowadays, industrial heat accounts for approximately three-quarters of the total energy demand in the industrial sector which is translated into 20% of the global energy consumption. This number corresponds to the total energy demand in the entire residential sector. Currently, most of these industrial heat needs are covered through fossil fuel combustion which results in a tremendous amount of direct CO_2 emissions. Only 9% of industrial heat is generated with renewable energy sources while the rest is divided between coal, natural gas, and oil depending on the specific industrial sector and its needs. In this context, industrial heat is usually divided into different categories depending on the temperature levels: Low-temperature heat below 150 °C, medium temperature heat between 150 °C and 400 °C and high-temperature heat above 400 °C, but other categorizations may also be found in literature.

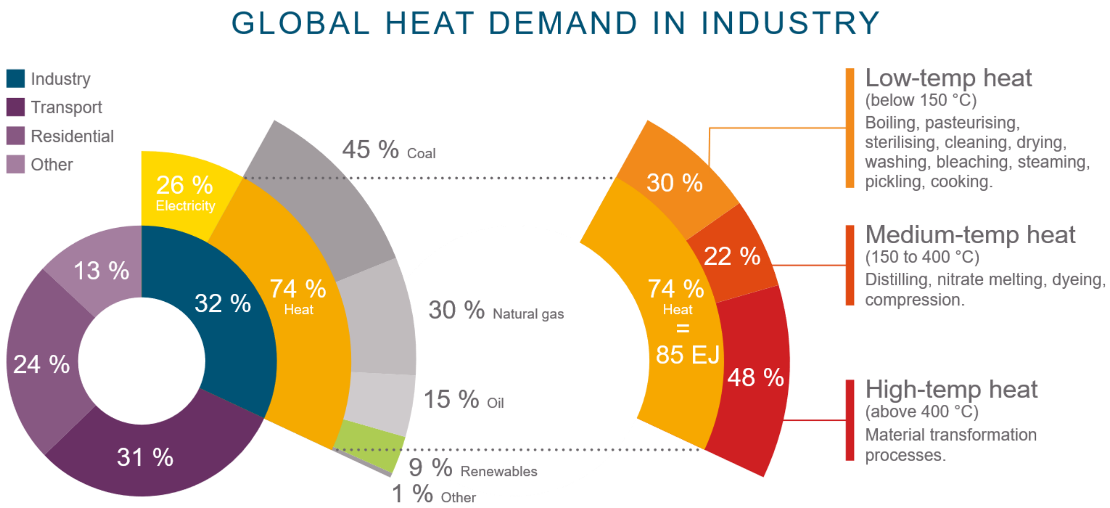

FIGURE 16. GLOBAL FINAL ENERGY CONSUMPTION BREAKDOWN AND HEAT DEMAND IN INDUSTRY

Some examples of industrial sectors that could use the low temperature heat generated at around 100 °C are the food and beverage, textiles, pulp and paper as well as pharmaceuticals industries. Likewise, medium to high temperature heat at around 500 °C could find customers in metal, ceramics, glass or chemical industries in processes such as melting and casting of metals, fining of ceramics, melting and forming of glass products or in various chemical processes. Finally, the so-called hard-to-abate industries are the ones usually requiring high-temperature heat for their processes which include for example the steelmaking processes, clinker production in cement kilns, certain processes in oil refining and others.

If cogeneration modes are to be considered in the current layout and operation, the total efficiency of the power plant could be increased and heat in various temperature levels could be generated, depending on the application. Three cogeneration scenarios are summarized in Figure 17. High temperature heat at around 760 °C could be extracted from the downstream flow from the REC and TES and before the Air – sCO2 heat exchanger. Such a cogeneration scenario would have an impact on the total electricity production and on the operation of the Air – sCO2 heat exchanger, if the high temperature heat is extracted on demand and not constantly. However, in this case the heat production can be decoupled from the power generation and the power plant's flexibility can be considerably increased. To still be able to operate the system close to design conditions if only heat is generated, we would need outlet air temperatures from the HEX close to the ones of the sCO2 based HEX. In general, it is worth highlighting that if the share between heat and power is very different and/or the working conditions of the two HEX are different then the inlet temperature to the receiver (and relative efficiency) would be affected. Another potential cogeneration scenario is the extraction of medium-high temperature heat in the range between 480 to 580 °C downstream of the air – sCO2 heat exchanger depending on the sCO2 power cycle layout. Subsequently, heat generation at this point will have an impact on the REC return temperature which will require a wide range of operating conditions for the receiver, in case that heat is extracted on demand and not continuously. Another impact would be a variation of the TES cold side temperature, which would also be subjected to wider operating ranges. A third cogeneration opportunity is associated with a heat extraction point before the sCO2 cooler in the power block which could provide low temperature heat of around 100 °C with an impact on the power generation cycle and the power block operation. One, two or a combination of these cogeneration opportunities could be realized depending on the desired power plant output.

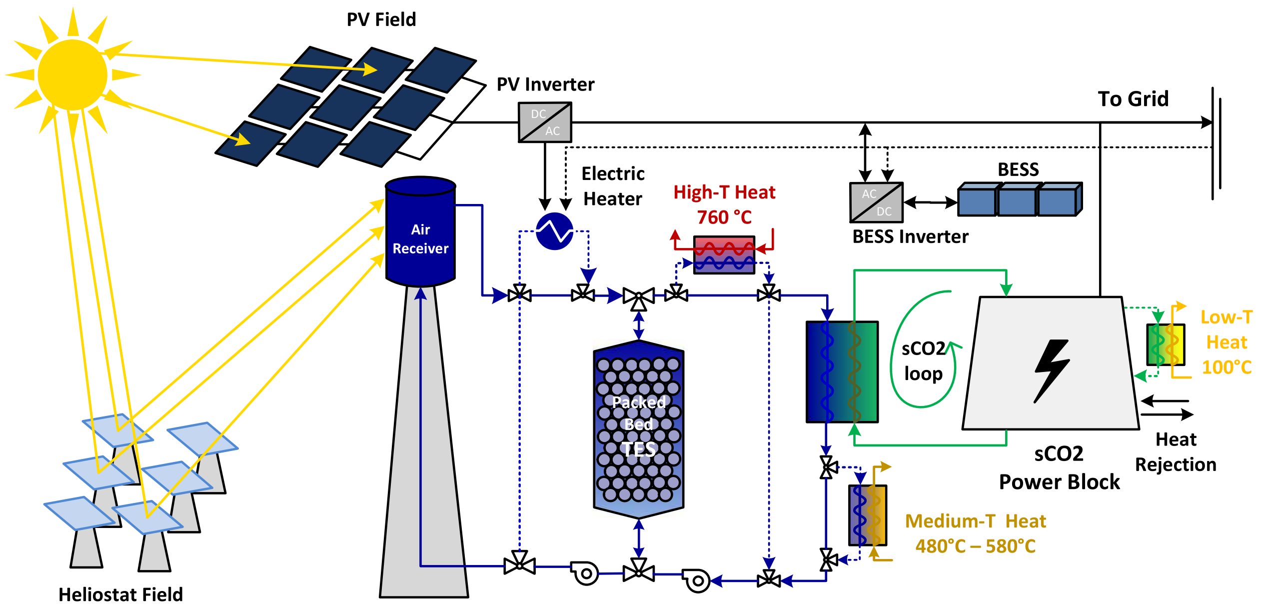

FIGURE 17. COGENERATION LAYOUT SCENARIOS

The power cycle layout also shows significant impact on the operation and cogeneration scenarios. A simple power cycle layout, such as the simple regenerated sCO2 Brayton cycle as depicted in paragraph 2.2 SHARP-sCO2 upscaled system: interfacing with solar field and power block, generally exhibits lower efficiencies compared to a configuration that incorporates recompression and intercooling (43% and 52% respectively as presented in Table 1). Simultaneously, the simpler layout boasts a lower specific cost and is easier to operate than the more complex one. It's crucial to note that as the efficiency of the layout increases, so does the return temperature of the sCO2, leading to a higher design cold temperature for the TES and air receiver. In systems incorporating cogeneration, as seen in Figure 17, the cycle's efficiency directly impacts the temperature of the medium temperature cogeneration. For instance, in a simple recuperated cycle, a medium temperature heat around 480 °C ($\Delta T_{HEX} \approx 217$ °C) may be considered, whereas a more efficient cycle could potentially recover up to 526 °C ($\Delta T_{HEX} \approx 174$ °C). If reheating is also considered as part of the power cycle, the medium temperature heat cogeneration could reach up to 580 °C. Subsequent techno-economic investigations can provide insights into whether maximizing plant revenues, with or without cogeneration, favors a more efficient or simpler cycle design.

4.1 TYPICAL OPERATION

To establish the control strategy for the power plant, two main approaches can be followed: a deterministic one and one utilizing a mixed-integer linear program (MILP) optimizer. The deterministic one is based on two main constraints: the non-dispatchable PV production is always prioritized, and the maximum power that can be injected into the grid is equal to the power block capacity. The optimized one is designed to either maximize revenues or minimize energy waste through its calculations. Figure 18 shows a summer week operation of the plant distinguishing thermal and electric thermal power production considering a deterministic operation. The thermal power production is driven by the CSP solar field (Q from REC), which operation follows the DNI profile unless the State of Charge (SOC) of the TES hits the maximum capacity. In that case, the solar field is defocused wasting potential thermal power production (Q_{Wasted}). During the daytime, the electricity production is driven by the PV (PV to Grid) and the sCO2 power block is in standby mode. If the AC electric power produced by the PV plant is above Pmax (considered as the maximum injectable power to the grid), the excess electric power contributes to charging the TES through the electric heater (PV to EH). If the TES is full, the AC excess power is wasted (PV to Waste). The power block is operated to compensate for the gap between the maximum power and the PV production. The small gap between PV and CSP electric power production is due to the limitation in minimum power to run the power block.

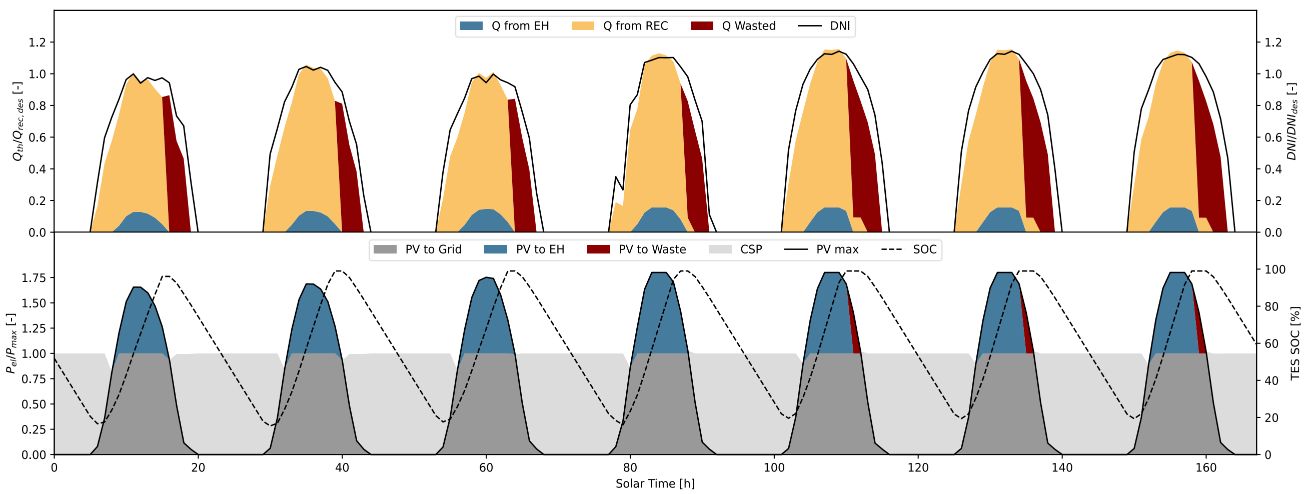

FIGURE 18. THERMAL AND ELECTRIC POWER PRODUCTION FOR A SUMMER WEEK

The detailed control logic flowchart adopted to manage the hybrid solar power plant is presented in Figure 19, and an example of application of these operating modes is presented for an average day in Figure 20. Depending on the actual DNI, the TES state of charge (SOC), and the PV electricity production, 9 different operating modes (OM) can be identified. Table 5 defines the operating modes, reporting the status of the PV field, the power block (PB), the receiver (REC), the electric heater (EH), the TES mass flowrate ($\dot{m}_{TES}$), and the power output (P_{out}). For the specified operation modes, it is crucial to consider operational limits, particularly concerning thermal components like the solar receiver, electric heater, and sCO_2 power cycle. To startup or shutdown, the solar receiver and electric heater, the threshold has been set at 20% of the design power. Regarding the part-load behavior of the sCO2 cycles, studies conducted under the SOLARSCO2OL project show that by regulating the rotational speed of the turbomachinery, nearly constant turbomachinery efficiencies can be maintained at partial loads above 40% of the nominal value. Consequently, the minimum operational condition of the power block has been set at 40%, ensuring consistent efficiency even during off-design operations.

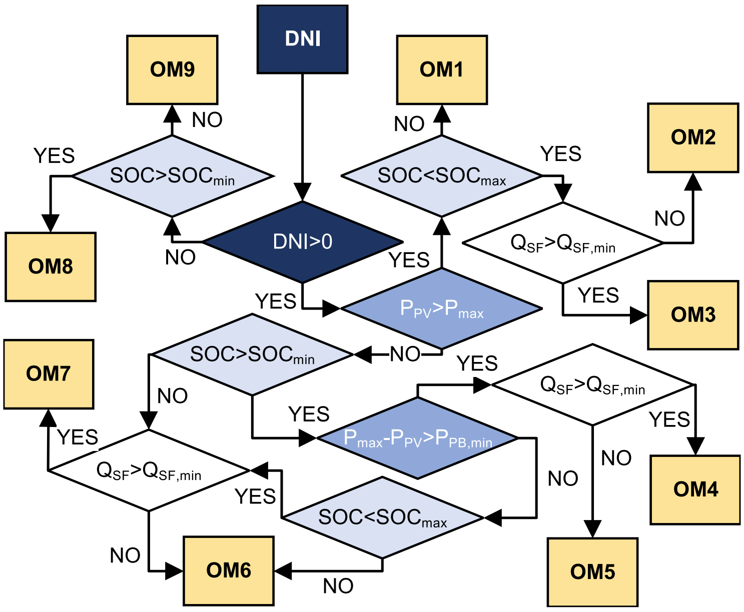

FIGURE 19. CONTROL LOGIC FLOWCHART

Specifically, OM1 occurs when only the PV system is generating electricity, exceeding the maximum power injectable to the grid. However, the TES is full, rendering the EH inactive, and the surplus production is wasted. On the other hand, OM2 involves the PV system reaching the maximum injectable power to the grid, with excess electrical power being converted to thermal power by the EH and stored in the TES. In both OM1 and OM2, the CSP solar field is non-operational. OM2 is an infrequent scenario, typically occurring only if an issue arises with the CSP solar field or if undergoes maintenance procedures. In OM1, the TES is full, causing excess electricity to be wasted, and the CSP solar field to be defocused. OM3 is a crucial scenario for PV and CSP hybridization, where the PV injects electricity into the grid, and both the EH and the CSP solar receiver generate thermal power stored in the TES. This scenario is common during summer operations, showcasing the value of EH and PV hybridization. OM4 and OM5 are similar, involving electricity production by both PV and the CSP power cycle. In OM4, the solar field is active, allowing the TES to potentially charge or discharge based on thermal power production and consumption. In contrast, OM5 occurs when the solar field is inactive, and the TES discharges to bridge the gap between the maximum grid-injectable power and PV production. Typically, OM5 follows OM4. Once the solar field stops generating, OM5 transitions to OM8, where only the CSP power cycle produces electricity, discharging the TES. OM6 is characterized by only PV generating electricity, while CSP is inactive either because the TES is empty (preventing the power cycle from running) or because the TES is full, necessitating the defocusing of the solar field, and at the same time, the gap between maximum power and PV production is not enough to run the power cycle. OM7 involves PV electricity production alongside the CSP solar field charging the TES. As mentioned earlier, OM8 signifies the operation mode where only the CSP power cycle produces electricity, discharging the TES. Lastly, OM9 represents a scenario with no electricity production, an empty TES, and both PV and CSP solar field being inactive.

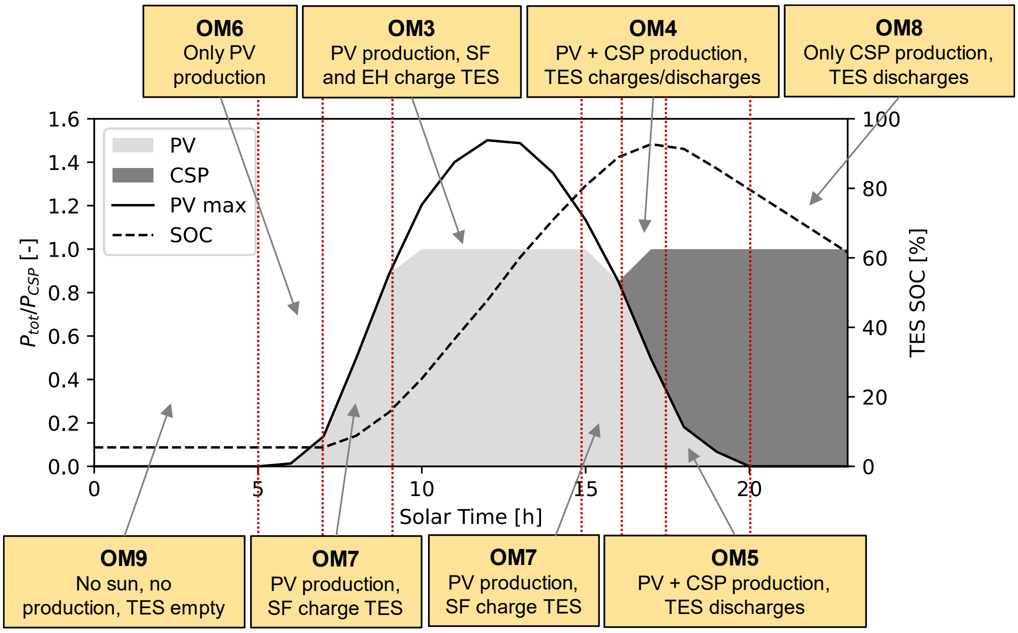

FIGURE 20. VISUALIZATION OF OPERATING MODES

TABLE 5: OPERATING MODES

OM	PV	PB	REC	EH	$P_{PV,wasted}$	$Q_{CSP,wasted}$	$\dot{m}_{TES}$	P_{out}
1	On	Off	Off	Off	> 0	> 0	0	P_{max}
2	On	Off	Off	On	0	> 0	$\dot{m}_{EH}$	P_{max}
3	On	Off	On	On	0	0	$\dot{m}_{rec} + \dot{m}_{EH}$	P_{max}
4	On	On	On	Off	0	0	$\dot{m}_{rec} - \dot{m}_{PB}$	P_{max}
5	On	On	Off	Off	0	0	$-\dot{m}_{PB}$	P_{max}
6	On	Off	Off	Off	0	0	0	P_{PV}
7	On	Off	On	Off	0	0	$\dot{m}_{rec}$	P_{PV}
8	Off	On	Off	Off	0	0	$-\dot{m}_{PB,des}$	P_{max}
9	Off	Off	Off	Off	0	0	0	0

Table 6 illustrates a qualitative operation mode transition matrix, employing colours to convey two key insights. Firstly, darker colours signify more frequent operation modes (e.g., OM7, OM8). Secondly, the intensity of colour at the intersection of two modes indicates the commonality of the transition between those modes. Consequently, it is evident that OM7 and OM8 are the predominant continuously generating modes, representing scenarios where only PV or only CSP is producing electricity. Notably, OM3, OM4, and OM5 are prevalent transition modes, with shorter durations, involving both CSP and PV. OM3 is particularly significant due to its frequent occurrence, demonstrating the value of the EH and the hybridization of PV. Conversely, OM1, OM6, and OM9 are considered more "extreme" modes as they activate when the TES reaches an extreme condition (full or empty), which happens less frequently and depends on seasonal variations. The transitions highlighted in Table 6 merit closer attention when modelling the plant's dynamics.

It is crucial to underline that the frequency of the respective operating modes depends on the specific power plant design such as the PV and CSP installed capacity. Certain boundary conditions can also alter the sequence of the OMs, such as the electricity price if considered in the dispatching strategy, but the main operating modes are expected to remain similar. The frequency of OM transitions depicted in Table 6 corresponds to a quasi-optimum power plant design.

TABLE 6: MOST COMMON TRANSITIONS BETWEEN OPERATING MODES

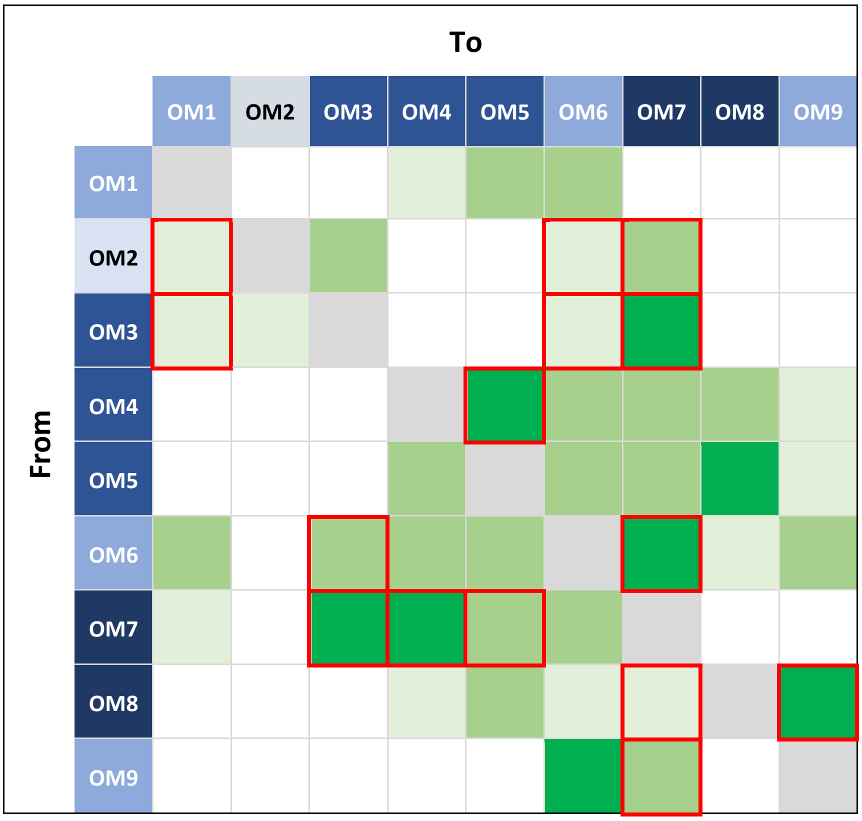

The operating modes transitions that require more attention for thermal components, so regarding electric heater, solar receiver and the power cycle (which directly affects the air-sCO2 HEx) are highlighted in the following summary. This main transitions are also highlighted in Table 6 where the relative cells have a red contour. It can be summarized that transitions with high occurrence (dark green) and elevated impact on the main components (red contour) are the main ones requiring deeper modelling and experimental validations.

Electric Heater	Start-up of the EH:	OM6→ OM2, OM3 OM7 → OM2, OM3
	Shut-down of the EH	OM2 → OM6, OM7, OM1 OM3 → OM6, OM7, OM1
Receiver	Start-up of the REC	OM9 → OM7 OM8 → OM7 OM6 → OM7
	Shut-down of the REC	OM4 → OM5 OM7 → OM5 OM3 → OM1
Power Block (air-sCO2 HEx)	Start-up of the PB	OM7 → OM4, OM5
	Rump-up/down of the PB	OM4 → OM5 OM5 → OM8
	Shut-down of the PB	OM8 → OM9

5 METHODOLOGY FOR SYSTEM MODELING AND MAIN KPIs

5.1 TECHNO-ECONOMIC MODELING METHODOLOGY

MoSES is a Python-based modeling tool, developed by KTH Royal Institute of Technology to estimate the techno-economic performance of hybrid PV-CSP power plants. A representation of the modeling methodology's flowchart is presented in Figure 21. The thermodynamic performance of the plant is estimated interconnecting the sub-systems quasi-steady-state models and integrating a CoolProp environment to estimate the properties of the fluids involved in the plant. Moreover, the NREL-PySAM wrapper for System Advisor Model (SAM) has been integrated into MoSES for designing the solar field and PV plant. The techno-economic performance of the system model is estimated by combining thermodynamics with an economic model based on a bottom-up estimation method. The resulting system model is customizable in terms of location (meteorological data, grid availability, electricity market, and economics of location), design assumptions, and dispatch strategy.

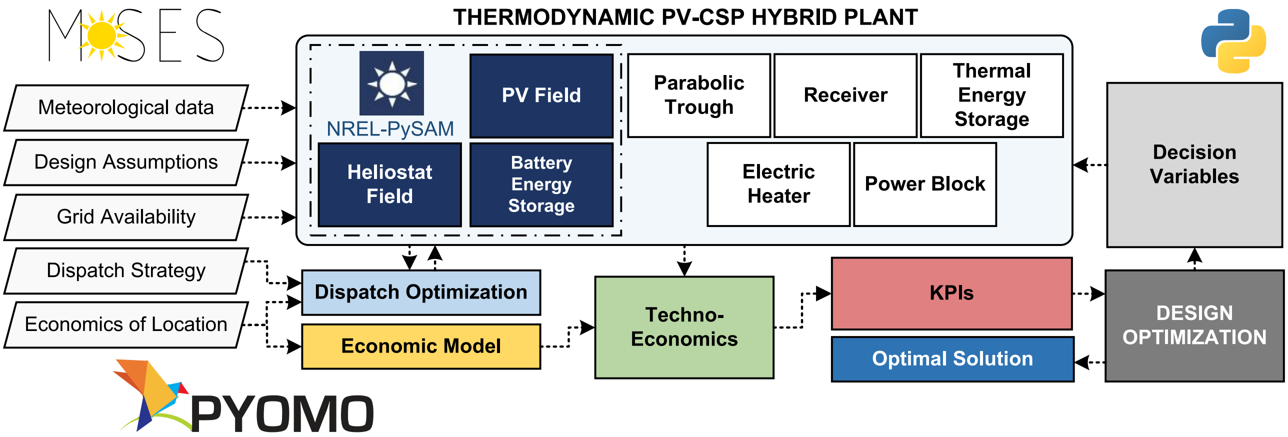

FIGURE 21. MOSES MODELLING METHODOLOGY FLOWCHART

To identify an optimal design of these hybrid solar plants a multi-objective optimization problem has been implemented so that a set of decision variables can be suggested to minimize/maximize user-selected objective functions such as Levelized Cost of Electricity (LCOE), Hybrid Capacity Factor (H-CF), Capital Expenditure (CAPEX), Annual Energy Yield (AEY), and maximum profit.

5.2 METHODOLOGY FOR DYNAMIC SYSTEM PERFORMANCE ANALYSIS

The Figure 22 reflects the methodology to be employed for the development of the system design at nominal conditions (a) and for the performance analysis on annual basis or at determined time intervals (b). The methodology includes the design and off-design models for each component and then integrating them into a system level model. All components models, including compressors, turbines, HEx, recuperators and dry-coolers, are based on the mass and energy balances at steady-state. The mathematical models are encoded in MATLAB. The working fluid properties are provided from REFPROP 9.1.

The methodology for the integration with the solar plant and receiver follows the structure and analysis of key parameters shown in Figure 11, deriving from the previous background published in Chen et al, 2022. The whole system design procedure starts from the power block side as it defines the required thermal power in receiver (oversized by the specified solar multiple). Both *IR* and T_{air} affect the receiver efficiency and thus the solar field design thermal power. These two parameters are main studied parameters and determine the optical-thermal-power integration of the whole SHARP-sCO2 system. Once the heliostat layout is determined with the help of SolarPILOT code, inclusion of the heliostat field operation is greatly simplified by using a solar field efficiency matrix, which maps the overall heliostat field efficiency over different sun positions.

Also, the effects of technical improvements in solar field and power block on the system performance and optimal *IR* will be quantified by varying the heliostat beam quality and main compressor inlet temperature MCIT (green hexagon in the figure).

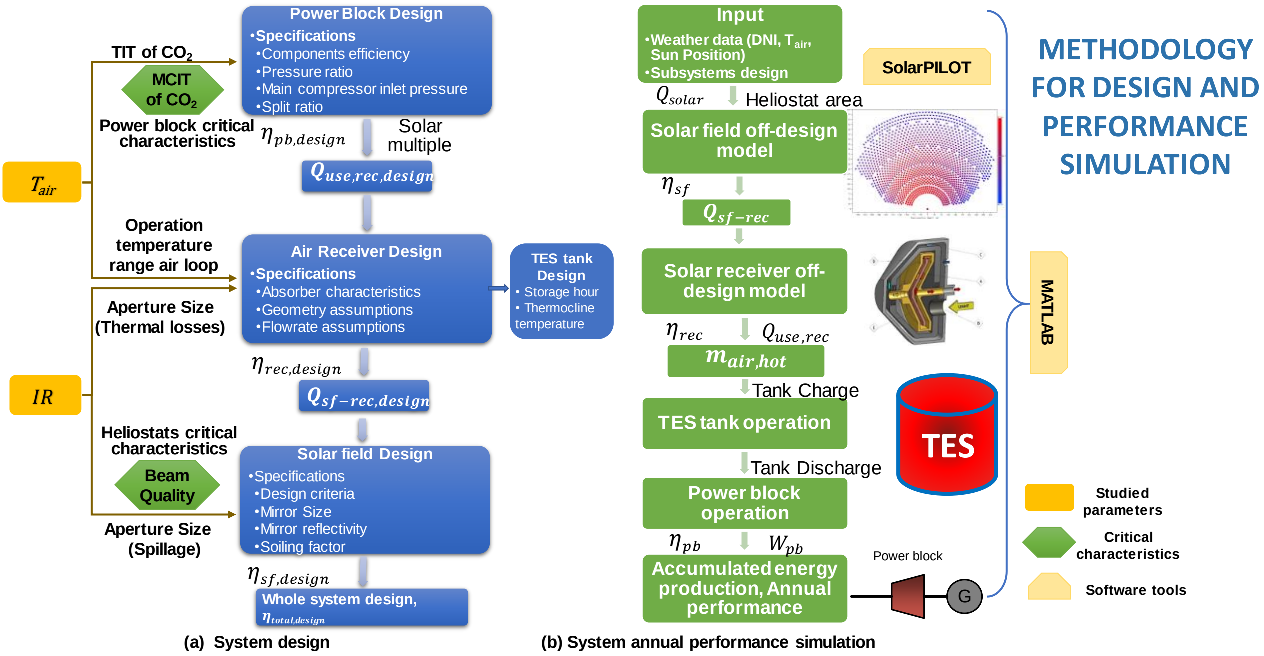

FIGURE 22. METHODOLOGY FOR SYSTEM PERFORMANCE ANALYSIS AT DESIGN POINT AND FOR ANNUAL OPERATION

The elaboration of annual system performance calculations requires control strategies in each subsystem to deal with the varying solar resource. Similar to the operation strategy used in molten salt receiver (https://sam.nrel.gov/weather-data), solar field is assumed to start to operate when DNI is above 200 W/m^2 and the solar elevation is higher than 8°. Solar receiver starts to work when the incident solar power exceeds 25% of the design power and the air mass flow rate is adjusted in response to the incident solar power to ensure that the outlet hot air is heated to the design temperature.

The total solar-to-electricity efficiency at design point (η_{total_design}) is the product of the efficiencies of all subsystems,

$$\eta_{total\_design} = \eta_{optic\_design} \cdot \eta_{thermal\_design} = \eta_{sf\_design} \cdot \eta_{rec\_design} \cdot \eta_{TES\_design} \cdot \eta_{pb\_design} \quad (1)$$

where η_{optic_design} represents the system optical efficiency at design point, $\eta_{thermal\_design}$ refers to the product of η_{rec_design} with η_{pb_design} and η_{TES_design}, and eventually the efficiency of the HEx, representing the global efficiency for transforming thermal to electrical energy.

The annual electricity generation (*E*) is calculated by Eq. (2), where *W(t)* is the power output from the power block during a specific hour interval. Like *E*, the annual energy reaching heliostat field (Q_{solar_annual}), receiver ($Q_{sf\text{-}rec\_annual}$) and TES (Q_{use,rec_annual}) are also the annual integral of the corresponding thermal power at each time step. The capacity factor (*CF*) can be determined by Eq. (3), where P_{pb} is the designed power block capacity (10 MW and 50 MW in this project).

$$E = \sum W(t) \cdot \Delta t \quad (2)$$

$$CF = \frac{E}{P_{pb} \cdot 8760} \quad (3)$$

The annual solar-to-electricity efficiency (η_{total_annual}) is the ratio of E to Q_{solar_annual}. Like η_{total_annual}, the η_{sf_annual} and η_{rec_annual} are the ratios corresponding to solar field and receiver respectively.

$$\eta_{total\_annual} = \frac{E}{Q_{solar\_annual}} \quad (4)$$

SHARP-sCO2 will customize the models of components and harmonization of comparisons for the specific technologies developed and will provide software tool of high value.

5.3 THERMODYNAMIC MODELS AND KPI OF MAIN COMPONENTS

The model of the complete system is based on component-level models at both design and off-design condition. Since by month 6 still some key components are under conceptual design, preliminary default thermodynamic models are herewith established as a reference and to be updated in revision by month 15.

Solar field layout optimization is developed in SolarPILOT (Wagner and Wendelin, 2018) while the receiver, storage tank+EH, HEx, power block and the whole system integration are modelled in MATLAB. Fluid properties of CO_2 and air are obtained from REFPROP.

5.3.1 SOLAR FIELD

The generation and performance characterization of solar field layouts are performed by SolarPILOT, which assesses the entire field performance by considering each heliostat individually. SolarPILOT firstly generates all possible heliostat positions based on the available land coordinates, tower height, and geometry of the heliostat and receiver by applying a determined layout generation algorithm. After simulating the performance of all heliostats at the design point, heliostats are sorted by their accumulated performance according to a user-defined criterion. The final field layout is composed of the most efficient heliostats that produce sufficient power to satisfy the solar field design thermal power.

Once the layout is designed, the incident solar power from the heliostat field on the receiver aperture, $\dot{Q}_{sf-rec}$, can be expressed as

$$\dot{Q}_{sf-rec} = \dot{Q}_{solar} \cdot \eta_{sf} = DNI \cdot A_{sf} \cdot \eta_{sf} \quad (5)$$

where $\dot{Q}_{solar}$ is the total solar power incident on the heliostats surface, *DNI* is the direct normal irradiance, A_{sf} is the heliostats area and η_{sf} is the total optical efficiency of the solar field, which can be represented by

$$\eta_{sf} = \eta_{cos} \cdot \eta_{surf} \cdot \eta_{sb} \cdot \eta_{att} \cdot \eta_{int} \quad (6)$$

where η_{cos} is the cosine efficiency, η_{surf} is the reflectivity and soiling efficiency, η_{sb} is the shadow and blocking efficiency, η_{att} is the atmospheric attenuation efficiency, and η_{int} is the intercept efficiency representing the spillage losses. Spillage is a factor strongly linking the optical performance of the heliostat field with the geometrical design of the receiver and more in particular the aperture area and tilt angle.

The KPI for optical efficiency of solar field at design point is of at least 70% and at least 62% on annual basis for the upscaled systems.

5.3.2 SOLAR RECEIVER

The solar receiver of SHARP-sCO2 presents a high degree of novelty not responding to the classical configuration of external cylindrical or cavity receivers. At present the concept is evolving to a tubular array rotor with a cylindrical aperture.

As a preliminary reference model by default, to be replaced by month 15 revision, it is proposed a typical cavity receiver, considering the relatively small power of the 10 MWe upscaled system. The design requires four main steps: (i) calculate parameters related to air mass flow rate and air properties; (ii) determine the receiver geometry based on a certain cavity angle and the required number of tubes; (iii) solve the heat transfer energy balance inside the absorber tubes by assuming tentative heat transfer coefficient; and (iv) evaluate the thermal losses according to the calculated tube surface temperature (T_{surf}).

The radiation heat loss $\dot{Q}_{loss,rad}$ is determined by a function of the receiver geometry, the emissivity of the tube material (ε_t) and refractory liner (ε_w), T_{surf}, and the ambient temperature (T_a), and it is obtained by the sum of the direct losses from the absorber panel to the aperture plus the radiation losses emitted by the refractory liner,

$$\dot{Q}_{loss,rad} = A_{ap} \cdot \left(\frac{\varepsilon_t}{\varepsilon_t + \dfrac{A_{ap}}{A_{abs}} \cdot (1-\varepsilon_t)}\right) \cdot \sigma \cdot (T_{surf}^4 - T_a^4) + \sum_{j=1} A_{ap} \cdot \varepsilon_w \cdot F_{j-ap} \cdot \sigma \cdot (T_{surf}^4 - T_a^4) \tag{7}$$

The radiation losses emitted by the refractory liner are accounted by utilizing the view factor between refractory liner surfaces (j) and the aperture (F_{j-ap}). F_{j-ap} is calculated by functions implemented in MATLAB. Part of the radiation from the refractory liner is directed to the absorber tubes and to themselves, and the rest escapes through the aperture. The temperature is assumed as equal inside the cavity. A_{ap} is the aperture area and σ represents the Stefan-Boltzmann constant.

Convection heat losses ($\dot{Q}_{loss,conv}$) considers the contributions from natural and forced convection, which mainly originate near the aperture and inside the cavity respectively. Due to the scarcity of experimental tests at high operating temperature, it is difficult to estimate the convective heat transfer coefficients accurately. According to the correlation presented by Kistler, 1986, $\dot{Q}_{loss,conv}$ can be calculated by Eq. (8),

$$\dot{Q}_{loss,conv} = (11.037 \cdot A_{abs} + 16.589 \cdot H_{ap}^{0.8}) \cdot (T_{surf} - T_a) + \sum_{j=1} 11.037 \cdot A_{w-j} \cdot (T_{surf} - (T_{surf} + T_a) \cdot 0.5) \tag{8}$$

where the natural convection between the absorber tubes and ambient is interpreted as the product of the absorber surface area (A_{abs}) and temperature difference between T_{surf} and T_a; the forced convection through the aperture to ambient is calculated by the function of the height of aperture (H_{ap}) and temperature difference between T_{surf} and T_a. Furthermore, the natural convection through refractory walls and the cavity shell to ambient air is also considered (represented in the second term of Eq. (8), A_{w-j} is the area of refractory liner j_{th}). With the assumption of homogeneous specular reflection of the incident radiation, the reflection losses ($\dot{Q}_{loss,refl}$) can be calculated by Eq. (9), where α_t and α_w are the absorptivity of the tube and the refractory liner, q_{rec} is the incident flux density on the absorber surface from the heliostat field. As refractory liner is usually made of low-absorbing materials, the fraction of radiation reflected from the refractory walls that passes through the aperture should be also taken into account,

$$\dot{Q}_{loss,refl} = (1-\alpha_t) \cdot q_{rec} \cdot A_{ap} + \sum_{j=1} (1-\alpha_t) \cdot q_{rec} \cdot (1-\alpha_w) \cdot F_{j-ap} \cdot A_{ap} \tag{9}$$

The receiver design procedure starts with an assumed $\dot{Q}_{use,rec}$ and ends with the calculation of the required $\dot{Q}_{sf-rec}$ as shown in Reyes-Belmonte et al, 2019. The geometry and thermal designs of the receiver are obtained by comparing the assumed $\dot{Q}_{use,rec}$ to the real $\dot{Q}_{use,rec}$, which results from the estimation of thermal losses. The receiver efficiency (η_{rec}) is shown as follows:

$$\eta_{rec} = \frac{\dot{Q}_{use,rec}}{\dot{Q}_{sf-rec}} = \frac{\dot{Q}_{sf-rec} - \dot{Q}_{loss,rad} - \dot{Q}_{loss,conv} - \dot{Q}_{loss,refl}}{\dot{Q}_{sf-rec}} \tag{10}$$

The off-design performance calculation follows the reverse iteration in the design procedure of the receiver. With a certain geometry design, the real incident flux $\dot{Q}_{sf-rec}$ is an input and determines the required mass flowrate of air to the desired temperature. Afterwards, T_{surf} and the corresponding thermal losses ($\dot{Q}_{loss,rad}$, $\dot{Q}_{loss,conv}$ and $\dot{Q}_{loss,refl}$) can be estimated. The off-design $\dot{Q}_{use,rec}$ and η_{rec} can then be calculated.

Receiver KPI are : Thermal power losses; Tin, Tout, air flowrate, pressure drop, power inlet onto aperture; peak flux, average flux, apparent emissivity and absorptivity (absorber and refractory); and part load efficiency.

The main KPI for the solar receiver is to achieve air outlet temperature > 800 °C, thermal efficiency > 80%, and pressure drop < 2%.

5.3.3 MAIN HEAT EXCHANGER AIR-TO-SCO2

The design of main heat exchanger HEx is by month 6 still under consideration. Design choice is essentially connected to available manufacturing capabilities and on scaleup options. A first selection of preferred variants were made to be further evaluated.

With a view to later upscaling, 3D printed solutions have been excluded by the moment. The preliminary selection includes: (Micro-) shell and tube hex or alternatively Plate- and fin configurations.

As a preliminary model by default, pending to update in the revision by month 15, it is decided to propose the use of the effectiveness-NTU method. As a reference it is adopted in this early stage a previous model adopted with S-shaped fin (Chen et al., 2021). By adopting periodic boundary conditions, the recuperator can be modelled as a single counter-flow channel unit. To consider the variations in thermophysical properties of sCO_2 , the channel unit is further discretized into sufficient heat exchangers sections along the channel length. The number of sub-heat exchangers depends on the extent of sCO_2 thermophysical properties variability. Outlet conditions on the hot side and cold side are estimated by knowing the inlet conditions on both sides and the desired value of recuperator effectiveness. Recuperator effectiveness (ε) is defined as the ratio between the actual heat flow transferred to the maximum achievable heat flow transferred, as shown in Eq. (11).

$$\varepsilon = \frac{C_h (T_{h,in} - T_{h,out})}{C_{\min} (T_{h,in} - T_{c,in})} \tag{11}$$

where C_h is the capacity rate of the hot stream, C_{min} is the minimum capacity rate of cold and hot streams, where the capacity rate is the product of the flow specific heat and the corresponding mass flow rate. $T_{h,\ in}$ and $T_{c,\ in}$ represent the inlet temperature of hot and cold stream respectively, and $T_{h,\ out}$ is the outlet temperature of hot stream. Enthalpy changes, in the whole recuperator, are estimated by assuming a pressure drop and, then, divided between each cell.

After calculating the heat exchanger performance with fixed effectiveness and fixed temperature difference, the conductance (UA) of these heat exchangers are further evaluated to compare the system complexity and characterize their off-design performance.

The conductance of heat exchanger can be obtained by the effectiveness-NTU method (Dyreby et al., 2014).

$$UA=\sum_{i=1}^{n} NTU_i \cdot C_{min} \tag{12}$$

$$NTU = \begin{cases} \dfrac{log\left(\dfrac{1-\varepsilon \cdot C_R}{1-C_R}\right)}{1-C_R} & if \quad C_R \neq 1 \\ \dfrac{\varepsilon}{1-\varepsilon} & otherwise \end{cases} \tag{13}$$

$$C_R = \frac{C_{min}}{C_{max}} \tag{14}$$

where *NTU* is the dimensionless number of transfer units for each division, C_{min} and C_{max} are the minimum capacitance rate and maximum capacitance rate of the hot and cold streams, respectively.

Important KPI for the primary heat exchanger are: Efectiveness; Tin and Tout (hot and cold sides); Heat transfer rate in each division; Pressure drop and Conductance (UA).

Main KPI is to operate the heat exchanger at air inlet temperature of up to 700 °C, achieve sCO2 outlet temperature of up to 650°C, effectiveness > 85% and pressure drop below 2%.

5.3.4 THERMAL ENERGY STORAGE AND ELECTRIC HEATER

Thermal Energy Storage system is to be based upon previous background of partner KTH on an innovative Radial-Flow High-Temperature Packed Bed Thermal Energy Storage (Trevisan et al., 2022) working at temperatures between 25 °C and 700 °C with a non-pressurized dry airflow. The lab will integrate the medium voltage high temperature EH upstream.

Considering the stored energy, E_{TES}, the charge and discharge efficiency and the round-trip efficiency are obtained as (Trevisan et al., 2022)

$$\begin{aligned} &\text{Charge efficiency} && \eta_{ch} = E_{TES}^{t_{ch}} / E_{IN,ch} \\ &\text{Discharge efficiency} && \eta_{disch} = \left(E_{OUT,disch} - E_{IN,disch}\right) / E_{TES}^{t_{ch}} \\ &\text{Total efficiency} && \eta_{tot} = \eta_{ch} \cdot \eta_{disch} = \left(E_{OUT,disch} - E_{IN,disch}\right) / E_{IN,ch} \end{aligned} \tag{15}$$

Main KPI of the TES+EH system are: Non-dimensional fluid temperature; Pressure drop; Thermocline thickness; Stored energy; State of charge; Charge efficiency; Discharge efficiency; Total efficiency; Utilization rate and temperature uniformity index. (See Trevisan et al. 2022, for details of KPI).

Fixed KPI for TES are to achieve air outlet temperature > 700 °C, round trip thermal efficiency > 70% and thermal exchange efficiency > 90%, limit pressure drop below 1%, and extend operation time at suitable outlet temperature to more than 70% of a full cycle duration.

Regarding EH, KPI are fixed to achieve air temperature > 850 °C, thermal efficiency > 95%, limit current leakage below 0.5%, and pressure drop below 2%.

5.3.5 POWER BLOCK

In SHARP-sCO2 project, the power block will be assessed only at a modelling level, in contrast with all the components forming part of the "cyber-physical" system (solar receiver, EH, TES and Hex) that will have their respective KPIs fully validated and measured in the different labs. The power block performance is evaluated based on the design and off-design point models from a previous study (Chen et al., 2021). Detailed component models were developed and validated in that study, including turbine, compressor, recompressor and low temperature and high temperature heat recuperators. The main compressor inlet pressure (MCIP) is determined by the MCIT to avoid the pinch point problem in the cold end of the low temperature recuperator. Split ratio of the mass flow rate of sCO_2 between the main compressor and the recompression is optimized by a genetic algorithm to maximize the power block efficiency (η_{pb}) under a certain TIT and MCIT. The heat exchanger that transfers the thermal energy from the hot air to the sCO_2 stream is the interfacing element between power block and SHARP-sCO2 solar thermal conversion system. For the purpose of modelling the downstream integration between Hex and PB, the reference sCO_2 temperature TIT will be 700 °C.

The radial compressor performance can be described by dimensionless flow and ideal head coefficients. The ideal head coefficient (ψ) and compressor off-design efficiency (η^*_c) are both functions of the flow coefficient (ϕ), and their functional relationships are expressed as (See Chen et al., 2021 for more details).

$$\phi = \frac{\dot{m}_{co_2,c}}{\rho_{in} U_c D_c^2} \left(\frac{N}{N_{design}}\right)^{1/5} \quad (16)$$

$$\psi = \frac{\Delta h_{ise}}{U_c^2} \left(\frac{N_{design}}{N}\right)^{(20\phi)^3} \quad (17)$$

$$\eta^*_c = \eta_{c,design} \left(\frac{N_{design}}{N}\right)^{(20\phi)^3} \quad (18)$$

where ρ_{in} is the density of sCO_2 at the compressor inlet, U_c is the tip speed of the rotor, D_c is the rotor diameter, N is the shaft speed, N_{design} is the design shaft speed, and Δh_{ise} is the isentropic enthalpy rise of the sCO_2 through the compressor.

Assuming most of the pressure drop is through the nozzles, the mass flow rate through the turbine is proposed in a first-order approximation:

$$\dot{m}_{co_2} = A_{nozzle} \cdot \rho_{out} \cdot C_s \quad (19)$$

where A_{nozzle} is the effective nozzle area of the turbine, ρ_{out} is the density of sCO_2 at the turbine outlet, and C_s is the spouting velocity, which is the velocity that will be achieved at the turbine outlet during an isentropic expansion:

$$C_s = \sqrt{2(h_{in} - h_{ise,out})} \quad (20)$$

The turbine off-design efficiency (η^*_t) is calculated by multiplying the aerodynamic efficiency (η_{aero}, that is the efficiency of an ideal turbine with no internal losses) by the turbine design point efficiency ($\eta_{t,\ design}$):

$$\eta^{*}_{t} = \eta_{t,design}\eta_{areo} = \eta_{t,design} 2v\sqrt{1-v^2} \quad (21)$$

where *v* is the velocity ratio, which is the ratio of rotor tip speed to spouting velocity.

5.4 TECHNO-ECONOMIC KPI AT SYSTEM LEVEL

Considering the SHARP-sCO2 integrated system the below KPIs will be taken into account when evaluating the solution techno-economic performance

Annual average Solar-to-Electricity efficiency (η_{STE}) [%]

The Solar-to-electric conversion efficiency measures the ability of the power plant to transform the primary solar resource into electricity. This PI can be calculated as the ratio between the total electric power produced in a year and the sum of the product of the irradiance (DNI) and the heliostat field area (A_{SF}) as in Eq. (22).

$$\eta_{STE} = \frac{\sum_{t=1}^{8760} W_{net}(t)}{\sum_{t=1}^{8760} DNI(t) \cdot A_{SF}} \quad (22)$$

Power Block design efficiency (η_{PB}) [%]

The power block efficiency measures the ability of the power block to convert thermal power into electric power at the design condition. This PI can be calculated at the design point as the ratio between the gross output electric power ($P_{gross,des}$) and the input thermal power (Q_{heater}) as in Eq. (23)

$$\eta_{PB} = \frac{P_{gross,des}}{Q_{heater}} \quad (23)$$

Capacity Factor (CF) [%]

The Capacity Factor is a measure of how much energy is produced by a plant compared to its design output (P_{nom}). It is calculated by dividing the total energy produced in a year by the amount of energy it would have produced if it ran at full output over that year, as in Eq. (24)

$$CF = \frac{\sum_{t=1}^{8760} W_{net}(t)}{P_{nom} \cdot 8760} \quad (24)$$

Electric Heater Utilization Factor (UF_{EH}) [%]

The electric heater utilisation factor is a KPI that identifies whether the capacity of the electric heater used for a particular configuration is too big or too small. It can be defined as the ratio between the total thermal energy produced and the maximum energy that could have been produced if the heater was utilized every day at nominal conditions ($Q_{EH,nom}$). The electric heater utilisation factor is calculated as in Eq. (25). Under this definition, a utilization factor of 100% means that the electric heater is used every day (24/7), possibly wasting electricity production in excess from the PV field. In that case, larger electric heater designs should be investigated. Conversely, lower utilisation values indicate the electric heater might be oversized when compared to the rest of the system.

$$UF_{EH} = \frac{\sum_{t=1}^{8760} Q_{EH}(t)}{Q_{EH,nom} \cdot 8760} \quad (25)$$

Annual Energy Yield (AEY) [GWh]

The annual energy yield provides the total annual electricity generation of the power plant. Considering a hybrid CSP+PV system, the AEY is calculated as the sum of the net electrical power generated by the power block ($W_{net,CSP}$) and the net power injected into the grid by the PV field $W_{net,PV}$ over one year as shown in Eq. (26).

$$AEY = \sum_{t=1}^{8760} \left[W_{net,CSP}(t) + W_{net,PV}(t) \right] \quad (26)$$

Annual Heat Yield (AHY) [GWh]

The annual heat yield provides the total annual heat generation of the power plant. Considering a hybrid CSP+PV system, the AHY is calculated as the sum of the net heat generation over one year as shown in Eq (27).

$$AHY = \sum_{t=1}^{8760} \left[Q_{net,CSP}(t) + Q_{net,PV}(t) \right] \quad (27)$$

PV-direct-share of Electricity Produced per Year (f_{PV}) [%]

The PV-share of AEY is a KPI that quantifies how much the PV-field impacts on the total electricity production of a hybrid PV+CSP plant. It is defined as the share between the sum of the PV net power injected into the grid $W_{net,PV}$ over the AEY as from Eq. (28)

$$f_{PV} = \frac{\sum_{t=1}^{8760} W_{net,PV}(t)}{AEY} \quad (28)$$

Capital Expenditure (CAPEX) [M€]

This KPI indicates the total investment required for the CSP plant or hybrid configuration CSP+PV for the different layouts under investigation, including direct and indirect costs. Direct costs include mainly the costs for the purchase and installation of the equipment (e.g. receiver, power block, thermal energy storage etc.). Indirect costs refer to the remaining costs incurred, for instance in connection to engineering, procurement and contingency during project development.

The direct CAPEX will be calculated using different equations for each layout under investigation depending on the considered components. A general formulation is shown in Eq. (29).

$$CAPEX_{direct} = (1 + f_{conting}) \cdot \left(C_{direct,CSP} + C_{direct,PV} + C_{direct,hybrid} \right) \quad (29)$$

The total direct cost is calculated taking into account the contingencies as a percentage of the direct cost ($f_{conting}$).

The indirect costs are estimated as in Eq. (30) considering the engineering, procurement, and construction factor, the decommissioning factor and the cost of the land.

$$CAPEX_{indirect} = \left(f_{EPC} + f_{decomm} \right) \cdot CAPEX_{direct} + C_{land} \quad (30)$$

Finally, the CAPEX is calculated as the sum of the total direct CAPEX and the indirect costs.

PV share of CAPEX ($f_{PV,CAPEX}$) [%]

The PV share of CAPEX quantifies the impact of the PV field on the total investment cost of a hybrid PV+CSP plant. It is defined as the share between the PV direct costs over the system direct costs.

Operational Expenditure (OPEX) [M€/year]

The OPEX relates to the operational and maintenance costs incurred during the operation of the power plant. These include fixed costs and production-dependent costs. The annual fixed cost and the specific operating and maintenance costs factor (operation dependent term) are assumed based on the specific layout under investigation.

Specific CAPEX (S_{CAPEX}) [€/MW]

The specific CAPEX is the investment cost per unit of installed capacity. This PI can be used to compare large-scale and small-scale configurations based on their investment cost identifying the relevance of economy of scale. The specific CAPEX is defined as in Eq. (31).

$$S_{CAPEX} = \frac{CAPEX}{P_{nom,CSP} + P_{nom,PV}} \quad (31)$$

Levelized Cost of Electricity (LCOE) [€/MWh]

The levelized cost of energy (LCOE) is a measure of cost per unit of electricity produced over the course of the lifetime of the plant. The LCOE considers all the cost sources into a single metric which is easy to understand and allows to compare alternative technologies with different scales of operation, different investment and operating periods. The LCOE can be calculated as presented in Eq. (32). considering the total capital and decommissioning expenditure, the annual operating expenditure, and the Annual Energy Yield. N is the expected lifetime of the system, while r is the discount rate.

$$LCoE = \frac{\sum_{t=1}^{n} \frac{CAPEX(t) + OPEX(t) + DECOMM(t)}{(1+r)^t}}{\sum_{t=1}^{n} \frac{AEY(t)}{(1+r)^t}} \quad (32)$$

Levelized Cost of Heat (LCOH) [€/MWh]

The levelized cost of energy (LCoH) is a measure of cost per unit of thermal energy produced over the course of the lifetime of the plant. The LCoH is a KPI similar to the LCoE but accounting for thermal energy production instead of power. The LCOH considers all the cost sources into a single metric which is easy to understand and allows to compare alternative technologies with different scales of operation, different investment and operating periods. The LCOH can be calculated as presented in Eq. (33). considering the total capital and decommissioning expenditure (for only the heat related components), the annual operating expenditure (for only the heat related components), and the Annual Heat Yield. This PI is considered for all layout whose main goal is thermal power production (or for layouts including cogeneration).

$$LCoH = \frac{\sum_{t=1}^{n} \frac{CAPEX_{heat}(t) + OPEX_{heat}(t) + DECOMM_{heat}(t)}{(1+r)^t}}{\sum_{t=1}^{n} \frac{AHY(t)}{(1+r)^t}} \quad (33)$$

Net Present Value (NPV) [M€]

The NPV is the sum of the discounted cash flows over the lifetime of the project. This PI is defined to compare different CSP layouts or hybrid CSP+PV configurations with the state-of-the-art tower CSP plant and investigate their profitability. The NPV is defined as in Eq. (34).

$$NPV = -CAPEX + \sum_{i=1}^{n} \frac{\left(\sum_{t=1}^{8760} \left[\lambda_{el}(t) \cdot W_{net}(t) + \lambda_{heat}(t) \cdot Q_{net}(t) \right] \right)_i - OPEX_i}{(1+r)^t} \quad (34)$$

Discounted Pay-Back period (DPB) [years]

The discounted payback period (DPB) is the number of years necessary to recover the project cost of an investment while accounting for the time value of money. DPB is exploited when risk is an issue (i.e., significant uncertainties are present) since it allows for a quick assessment of the duration during which an investor’s capital is at risk.

CONCLUSIONS

WP5 addresses one of the main objectives of the SHARP-sCO2 project: to develop and validate (via a cyber-physical cycle approach) at TRL 5 an innovative air-driven CSP cycle to be hybridized with PV towards LCOE minimisation. The virtual laboratory is formed by hardware physically located and tested in three different labs. Given the distributed configuration of the system, the integration cannot be fully optimized because of constraints imposed by the different test benches. Since an integrated test is also not possible, the validation should be implemented by a harmonized interfacing of inputs and outputs of the different components. The main purpose of this D5.1 is to identify the most relevant SHARP-sCO2 layouts to ensure an agreement on the interfacing points and key boundary conditions for the dialogue between main components to be developed in the project and also guiding the technical specifications for the upscaled systems to be analysed in WP5.

Simple regeneration and recompression cycles are adopted as reference cycles for the end-use of CST converted by SHARP-sCO2 technology with tentative reference TIT of 680 °C and a sCO_2 TI at the exit of the HEx of 700 °C. Following reverse cascade thermal steps, it is provided the boundary conditions established for temperature gradients from the solar receiver and EH outputs (800-850 °C) to the HEx (700 °C). The interfacing list of parameters establishes also common figures for pressures and flowrates in the components conforming the cyberphysical system. The introduction of hybridization with PV and cogeneration is also addressed highlighting their main influence over the system operation and performance.

Considering design and off-design optical interfacing with typical characteristics of heliostat fields, the use of standard heliostat beam quality and the ambient air temperatures for the power block corresponding to Morocco, it is agreed typical IR values between 1,200-1,500 kW/m^2 onto receiver aperture.

The deliverable provides the structure to be used for the methodology of simulation of the integrated system and formulates reference thermodynamic models for the main components as well as KPIs for the overall integrated system.

REFERENCES

Chen R, Romero M, González-Aguilar J, Rovense F, Rao Z, Liao S. Design and off-design performance comparison of supercritical carbon dioxide Brayton cycles for particle-based high temperature concentrating solar power plants. Energy Convers Manag 2021;232:113870. https://doi.org/10.1016/j.enconman.2021.113870.

Chen R, Romero M, González-Aguilar J, Rovense F, Rao Z, Liao S. Optical and thermal integration analysis of supercritical CO2 Brayton cycles with a particle-based solar thermal plant based on annual performance. 2022, Renewable Energy, 189, 164-179

Dyreby J, Klein S, Nellis G, Reindl D. Design considerations for supercritical carbon dioxide brayton cycles with recompression. J Eng Gas Turbines Power 2014;136. https://doi.org/10.1115/1.4027936.

Kistler BL. A user's manual for DELSOL3: A computer code for calculating the optical performance and optimal system design for solar thermal central receiver plants. 1986. Pages: 231. https://doi.org/SAND86-8018.

Reyes-Belmonte MA, Sebastián A, Romero M, González-Aguilar J. Optimization of a recompression supercritical carbon dioxide cycle for an innovative central receiver solar power plant. Energy 2016;112:17–27. https://doi.org/10.1016/j.energy.2016.06.013.

Reyes-Belmonte MA, Sebastián A, Spelling J, Romero M, González-Aguilar J. Annual performance of subcritical Rankine cycle coupled to an innovative particle receiver solar power plant. Renew Energy 2019;130:786–95. https://doi.org/10.1016/j.renene.2018.06.109

Trevisan S, Wang W, Guedez R, Laumert B. Experimental Evaluation of an Innovative Radial-Flow High-Temperature Packed Bed Thermal Energy Storage. Appl Energy 2022;311. https://doi.org/10.1016/j.apenergy.2022.118672.

Wagner MJ, Wendelin T. SolarPILOT: A power tower solar field layout and characterization tool. Sol Energy 2018;171:185–96. https://doi.org/10.1016/j.solener.2018.06.063.

MECHERI Mounir (2018) *D1.1 – sCO2 Brayton cycle architecture and components' specifications*. Available at: https://www.sco2-flex.eu/wp-content/uploads/2019/06/D1.1-–-sCO2-Brayton-cycle-architecture-and-components'-specifications.pdf (Accessed: 15 January 2024).